



University of Kentucky
UKnowledge

Theses and Dissertations--Mechanical
Engineering

Mechanical Engineering


2020

INFLUENCE OF SIZE EFFECTS ON SURFACE GENERATION DURING FINISH MACHINING AND SURFACE INTEGRITY IN TI-6AL-4V

Ian S. Brown

University of Kentucky, iansbrowninc@gmail.com

Author ORCID Identifier:

 <https://orcid.org/0000-0001-9229-3119>

Digital Object Identifier: <https://doi.org/10.13023/etd.2020.361>

[Right click to open a feedback form in a new tab to let us know how this document benefits you.](#)

Recommended Citation

Brown, Ian S., "INFLUENCE OF SIZE EFFECTS ON SURFACE GENERATION DURING FINISH MACHINING AND SURFACE INTEGRITY IN TI-6AL-4V" (2020). *Theses and Dissertations--Mechanical Engineering*. 157. https://uknowledge.uky.edu/me_etds/157

This Master's Thesis is brought to you for free and open access by the Mechanical Engineering at UKnowledge. It has been accepted for inclusion in Theses and Dissertations--Mechanical Engineering by an authorized administrator of UKnowledge. For more information, please contact UKnowledge@lsv.uky.edu.

STUDENT AGREEMENT:

I represent that my thesis or dissertation and abstract are my original work. Proper attribution has been given to all outside sources. I understand that I am solely responsible for obtaining any needed copyright permissions. I have obtained needed written permission statement(s) from the owner(s) of each third-party copyrighted matter to be included in my work, allowing electronic distribution (if such use is not permitted by the fair use doctrine) which will be submitted to UKnowledge as Additional File.

I hereby grant to The University of Kentucky and its agents the irrevocable, non-exclusive, and royalty-free license to archive and make accessible my work in whole or in part in all forms of media, now or hereafter known. I agree that the document mentioned above may be made available immediately for worldwide access unless an embargo applies.

I retain all other ownership rights to the copyright of my work. I also retain the right to use in future works (such as articles or books) all or part of my work. I understand that I am free to register the copyright to my work.

REVIEW, APPROVAL AND ACCEPTANCE

The document mentioned above has been reviewed and accepted by the student's advisor, on behalf of the advisory committee, and by the Director of Graduate Studies (DGS), on behalf of the program; we verify that this is the final, approved version of the student's thesis including all changes required by the advisory committee. The undersigned agree to abide by the statements above.

Ian S. Brown, Student

Dr. Julius M. Schoop, Major Professor

Dr. Alexandre Martin, Director of Graduate Studies

INFLUENCE OF SIZE EFFECTS ON SURFACE GENERATION DURING FINISH
MACHINING AND SURFACE INTEGRITY IN TI-6AL-4V

THESIS

A thesis submitted in partial fulfillment of the
requirements for the degree of Master of Science in
Mechanical Engineering in the College of Engineering
at the University of Kentucky

By

Ian Samuel Brown

Lexington, Kentucky

Director: Dr. Julius M. Schoop, Professor of Mechanical Engineering

Lexington, Kentucky

2020

Copyright © Ian Brown 2020

<https://orcid.org/0000-0001-9229-3119>

ABSTRACT OF THESIS

INFLUENCE OF SIZE EFFECTS ON SURFACE GENERATION DURING FINISH MACHINING AND SURFACE INTEGRITY IN TI-6AL-4V

Finish machining is an essential manufacturing process that is used to enhance the mechanical characteristics of critical components. The deformation that occurs at the tool and workpiece interface in finish machining significantly affects a host of component properties, commonly referred to as “surface integrity” properties. Surface roughness is a machining deformation-affected characteristic that is of high relevance in contemporary manufacturing. However, over recent decades it has been made clear that the material properties of the deformed surface layers are relevant to component performance as well. Predicting the overall surface quality of a machined component is of great relevance to the manufacturing industry.

Current state-of-the-art predictive models in the area of machining-induced surface integrity are typically founded in two-dimensional F.E.M. analysis. These investigations frequently show the advantages of tool geometry manipulation. However, most efforts focus solely on the prediction of two-dimensional surface integrity qualities such as those found in orthogonal machining. Indeed, most recent models largely ignore three-dimensional properties such as surface roughness, and do not incorporate three-dimensional machining parameters that are highly relevant to the surface integrity state of typical finished components. In light of these shortcomings, the nature of surface integrity in three-dimensional machining is explored, and a physics-based geometric model of surface generation is applied to some areas of surface integrity prediction.

The main focus of this work is to investigate and model the relationship between the more dominant parameters in finish turning (feed, nose radius, and edge geometry) and the surface generation phenomena that occur in the application of tools with varied geometries of this scope. The presented geometric model is derived from unique assumptions that allow for the close approximation of surface generation. The model is subsequently validated with experiments that utilize modified turning inserts of precise edge geometry, as well as pedigreed data from previous literature. Good agreement with

experimental roughness results is obtained, thus verifying the validity of the surface generation assumptions. In addition, subsurface properties are found to correlate well with the geometry of ploughed areas predicted by the modeling methodology presented in this text.

KEYWORDS: Surface Integrity, Material Side Flow, Minimum Uncut Chip Thickness, Finishing, Multi-Path, Size Effect

Ian Samuel Brown

(Name of Student)

08/5/2020

Date

INFLUENCE OF SIZE EFFECTS ON SURFACE GENERATION DURING FINISH
MACHINING AND SURFACE INTEGRITY IN TI-6AL-4V

By
Ian Samuel Brown

Dr. Julius M. Schoop

Director of Thesis

Dr. Alexandre Martin

Director of Graduate Studies

08/5/2020

Date

ACKNOWLEDGMENTS

I would like to show great appreciation to my advisor, Dr. Julius Schoop, whose patient mentorship was the cornerstone of my academic and professional growth during this effort. The skills and knowledge that Dr. Schoop has imparted to me during my research have significantly advanced my ability to answer complex problems in metal cutting and manufacturing as a whole. Without this guidance, none of what I have achieved in this work would have been possible.

Furthermore, I would like to graciously thank my committee members, Dr. I. S. Jawahir and Dr. Matthew Beck, for being involved in this work. I am grateful for their interest, and for the time, support, and valuable expertise they have provided.

Other various University of Kentucky staff have been instrumental to my success as well. In particular, Dana Harrod, Nicolas Briot, and Adam Price provided exceptional support and expertise during my research.

Throughout my graduate career, I have been blessed to have collected a great group of lab mates, coworkers, and friends, including David Adeniji, Jason Wolf, James Caudill, Melissa Anders, Yangyang Wu, Shehan Gunawardena, Clayton O'Donoghue and Will Platou. I am grateful for the priceless technical assistance this group has given me, and for the less rigorous conversations we have had along the way. Special thanks are due to the undergraduates of this group, Shehan Gunawardena, Clayton O'Donoghue and Will Platou, who spent many hours of their own time to help complete this work.

I would also like to thank two industry contacts, George Adinamis and Raja Kountanya, for showing interest in this work, asking pertinent questions, and providing opportunities to share and discuss the discoveries made during my studies.

Finally, I would like to give the utmost thanks to my family, who have been unwavering in their support and confidence during my entire academic career. Specifically, I would like to thank my parents effusively. Without their guidance, patience, and sacrifice, I would not have been able to complete this journey.

TABLE OF CONTENTS

ACKNOWLEDGMENTS	iii
LIST OF TABLES	vi
LIST OF FIGURES	vii
CHAPTER 1. Introduction.....	1
CHAPTER 2. Technical Background and Previous work	3
2.1 <i>Finish Machining Principles</i>	3
2.1.1 Motivation	3
2.1.2 Surface Generation Basics.....	5
2.1.3 Surface Topography	6
2.1.4 Subsurface Properties	8
2.2 <i>Surface Generation and Surface Integrity in Finish Machining</i>	9
2.2.1 Surface Roughness	9
2.2.2 Subsurface Properties	14
2.2.2.1 Hardness.....	17
2.3 <i>Closing Statements</i>	19
CHAPTER 3. Equipment and Procedures	21
3.1 <i>Finish Turning</i>	21
3.1.1 Cutting Edge Honing	23
3.2 <i>Sample Characterization</i>	24
3.2.1 Sample Cross Section Preparation.....	27
3.2.2 Scanning White Light Interferometry.....	29
3.2.3 Electron and Focused Ion Beam Microscopy	29
3.2.4 Optical Microscopy	30
3.2.5 Microhardness Evaluation	31
3.2.6 Nanoindentation	32
3.3 <i>Model Development</i>	33
CHAPTER 4. Surface Generation Model Development.....	34
4.1 <i>Assumption Development</i>	34
4.2 <i>Surface Roughness Simulation of Surfaces Generated by Lambert-Inspired Assumptions</i>	35
4.2.1 Validation of Simulated Surface Roughness	39
4.2.2 Incorporation and Validation of Machine Tool Error Dynamic Offset	42
4.3 <i>Subsurface Integrity Case Study Correlated to Surface Generation Model Geometry</i>	47
4.3.1 Subsurface Microhardness.....	48
4.3.2 Subsurface Hardness Variations in Feed Direction	57
CHAPTER 5. Conclusions and Outlook.....	60
5.1 <i>Future Work</i>	62

APPENDIX.....	63
REFERENCES	76
VITA.....	81

LIST OF TABLES

Table 2.1. Different levels of surface integrity data sets for the inspection of machined components (modified from [2] with permission of Elsevier Inc., submission ID 1035201).	15
Table 3.1. Experimental Parameters and Levels.....	22
Table 3.2. Polishing Regimen.....	27
Table 3.3. Kroll's Reagent Use.....	28
Table 4.1. Material properties, and empirically determined material-specific y_{eff} and h_{min}/r_e values for the workpieces studied.....	39

LIST OF FIGURES

Figure 2.1. Surface roughness produced by common methods (modified from [2] with permission of Elsevier Inc., submission ID 1035201).....	4
Figure 2.2. (a) Three-dimensional model of basic turning geometry; (b) cross section of the three-dimensional model displayed on the left. Note the presence of affected subsurface area denoted by dashed lines.	6
Figure 2.3. Illustration for the calculation of Roughness Average R_a	6
Figure 2.4. Basic turning surface generation geometry showing the replication of the tool corner radius onto the workpiece.	7
Figure 2.5. (a) Simulated surface from turning, created assuming perfect chip removal; (b) Simulated surface created by assuming material in the Spanzipfel region is left on the surface and behaves elastically. Adapted from author’s published work with permission from MDPI [16].	11
Figure 2.6. Simulated surface created by assuming some constant amount of material is pushed to the side during each tool pass. Adapted from author’s published work with permission from MDPI [16].	12
Figure 2.7. Chart of material properties that are relevant to failure types. (reproduced from [53] with permission of Elsevier Books Limited, reference number 40346, originally modified from[52], with permission of Elsevier Inc., license number 4875501237893).	16
Figure 2.8. The effect of dressing conditions on observed microhardness induced by grinding (reproduced from [52] with permission of Elsevier Inc., license number 4875501237893).	18
Figure 3.1. (a) HAAS TL2 CNC lathe used to perform cutting tests; (b) Kennametal TPGN K-68 tool of $r_c = 0.8$ mm tool being touched off the Ti-6Al-4V workpiece. Adapted from author’s published work with permission from MDPI [16].	21
Figure 3.2. The three turning tool types used, and the face turned samples.	22
Figure 3.3. (a) Image of the tooling and workpiece geometry created for the tool honing program; (b) CNC milling machine interior, equipped with buffing wheel impregnated with 1 μ m diamond paste, carbide turning tool is held in place by a tool and vise.	23
Figure 3.4. (a) Rake face view of modified edge of a Kennametal TPGN K-68 tool of $r_c = 3.2$ mm, $r_e = 30$ μ m; (b); Tool cloudmap produced via scanning white light interferometer; (c) Subsequent analysis of tool cloudmap via MATLAB; (d) Used tool exhibiting tool/workpiece contact discoloration and limited adhesion, but no tool- (edge- or nose-) wear. Adapted from author’s published work with permission from MDPI [16].	24
Figure 3.5. Metallographic sample analysis geometry clarification.	26
Figure 3.6. Typical results of polishing, (a) viewed optically with polarized light; (b) viewed optically after etching.	28
Figure 3.7. Comparison of two grain-viewing methods: (a) polarized light; (b) etching with Kroll’s Reagent.	29
Figure 3.8. (a) Optical image of the geometry produced by the FIB “skimming” method of revealing the near surface microstructure; (b) SEM micrograph showing the resulting skimmed material in better definition.	30

Figure 3.9. Microhardness indents created by a Vickers indenter. One indent is placed within a large grain. The left indent, placed in an average grain of $\sim 10 \mu\text{m}$ diameter, gave a hardness value of 297.1 HV, while the right indent gave a value of 262.2 HV.	32
Figure 3.10. Example of nanoindent matrix on a metallographically polished sample, representative of the indentation matrices performed on all investigated samples.	33
Figure 4.1. (a) Initial model workpiece geometry; (b) Tool geometry imposed on the previously defined workpiece geometry. Adapted from author's published work with permission from MDPI [16].	36
Figure 4.2. (a) Tool geometry imposed on new surface profile, altered by the current tool pass; (b) Magnified examples of the model geometry that clarify the side flow transition and surface profile construction. Adapted from author's published work with permission from MDPI [16].	37
Figure 4.3. (a) Tool geometry in new pass position imposed on the surface profile generated by the previous pass; (b) Surface profile created by the iterative model, shown at equilibrium. Adapted from author's published work with permission from MDPI [16].	38
Figure 4.4. Surface profile created by the iterative model, shown at equilibrium after gaussian filtering. Adapted from author's published work with permission from MDPI [16].	38
Figure 4.5. Roughness (R_z) model (lines) compared to data gathered through experimental investigation in Ti-6Al-4V. Adapted from author's published work with permission from MDPI [16].	40
Figure 4.6. Model compared to data adapted from Knuefermann [13], roughness measurements were taken in both long and short formats to show waviness influence on the typical long measurements. Material: 51CrV4. Adapted from author's published work with permission from MDPI [16].	41
Figure 4.7. Surface profile altered by MTE, typical of way axis-induced error. Adapted from author's published work with permission from MDPI [16].	43
Figure 4.8. (a) Tool/workpiece interface model depicting the tendency of a small edge radius to promote less MTE damping (b) Tool/workpiece interface model depicting the tendency of a large edge radius to result in more MTE damping, proportional to the increase in h_{min} . Adapted from author's published work with permission from MDPI [16].	44
Figure 4.9. Model compared to data adapted from Childs [4], MTE-induced roughness is predicted with some accuracy. Material: Al 1075. Adapted from author's published work with permission from MDPI [16].	46
Figure 4.10. (a) Surface model showing the tool profile depth and light overlapping of previous passes, modeled with $r_c = 0.4 \text{ mm}$, $h_{min} = 5 \mu\text{m}$, and $f = 0.1 \text{ mm}$; (b) Surface model showing heavy multi-pass condition, modeled with $r_c = 1.6 \text{ mm}$, $h_{min} = 5 \mu\text{m}$, and $f = 0.1 \text{ mm}$. Adapted from author's published work with permission from MDPI [16].	48
Figure 4.11 Etched and FIB-skimmed samples showing the relative lack of microstructural damage occurring at (a) gentle conditions and; (b) relatively abusive conditions.	49

Figure 4.12. (a) Microhardness profile of surface with slight thermal softening;(b) microhardness profile of surface with moderate strain hardening.....	50
Figure 4.13. (a) Microhardness profile of surface with thermal softening;(b) microhardness profile of surface with slight thermal softening.....	51
Figure 4.14. (a) Microhardness profile of surface with substantial thermal softening;(b) microhardness profile of surface with significant apparent strain hardening.	53
Figure 4.15. Determination of the ploughing constant for a given surface.	54
Figure 4.16. Hardness trends plotted against tool edge radius for $f=0.2$ mm (a) model predicted ‘ploughing constant’ and (b) observed microhardness data. Relative hardness alteration is of small magnitude due to large f	55
Figure 4.17. Hardness trends plotted against tool edge radius for $f=0.1$ mm (a) model predicted ‘ploughing constant’ and (b) observed microhardness data. Relative hardness alteration is of large magnitude due to small f	56
Figure 4.18. Three-dimensional subsurface hardness profile for machining conditions: (a) $r_c = 0.4$ mm, $f=0.1$ mm, $r_e = 12.5$ μm ; (b) $r_c = 0.8$ mm, $f=0.2$ mm, $r_e = 30$ μm	58
Figure 4.19. (a) Three-dimensional subsurface hardness profile for machining conditions: $r_c = 1.6$ mm, $f=0.2$ mm, $r_e = 20$ μm ; (b) magnified model subsurface geometry for this condition.	59

CHAPTER 1. INTRODUCTION

Finish machining is a longstanding process in the manufacturing industry that is dominant among all processes in the production of precise surfaces. This methodology allows manufacturers to create parts with specific surface qualities, typically tailored for use in precision applications such as aerospace, automotive, or biomedical industries. While the current practice of many manufacturers is to investigate and verify these critical qualities experimentally, research in recent decades has been focused on eliminating the time and cost of experimentally determining the most advantageous machining parameters by modeling machining-induced “surface integrity”. However, the finish machining process is complex, and is subject to the repercussions of many process-specific “size effects”, due to exacerbated material ploughing encountered at the cutting edge in the finishing regime. Thus, modeling of surface integrity in finish machining is non-trivial, as confirmed by the inaccuracies of many modern machining models [1].

Contemporary modeling of surface integrity in machining is most often investigated by simplifying the machining case to two dimensions: cutting and depth of cut directions. This simplification applies directly to orthogonal turning and allows for easier calculation and study of the thermo-mechanical phenomena that occur in this plane, that in turn affect surface integrity. F.E.M is the model type primarily employed in this way, and allows for the calculation of stresses, strains, and material alterations that arrive from these phenomena. While much progress has been made in the prediction capabilities of these models, the material constitutive relationships and assumptions applied within the framework of these models are difficult to obtain, and error prone. Moreover, the simplification of machining into two dimensions ignores process parameters that significantly influence surface integrity. Thus, F.E.M. or other two-dimensional methods have yet to be highly utilized in industry. Nonetheless, the pursuit of two-dimensional prediction capabilities for surface integrity values is certainly relevant as a basis for understanding machining process mechanics.

Alternative to the two-dimensional case, prediction of surface integrity arriving from the nuances of three-dimensional processes has been studied very little, given its additional complications. While the general surface integrity trends predicted by two-

dimensional models do carry over to the three-dimensional case, to what extent and form is practically unknown. Additionally, three-dimensional surface integrity metrics such as surface roughness, and subsurface material property variations in the feed direction have largely been ignored by contemporary efforts. Furthermore, surface roughness is highly influenced by cutting edge radius - one of the commonly varied factors of two-dimensional modeling - yet few recent roughness models have considered this highly relevant parameter.

This thesis is focused on investigating the influence of machining parameters on surface generation phenomena in the finish machining of ductile materials. It is hypothesized that surface integrity values may be directly correlated to geometric machining parameters, and that a geometry-based surface generation model can predict the surface integrity behavior resulting from these varied conditions. Through the use of modified carbide turning tools, the parameters feed, corner/nose radius, and cutting edge radius are varied in a series of turning tests. A host of analysis techniques are utilized to illuminate the relevance of each parameter on the machined surface integrity found under these conditions. Concurrently, a geometrical model is developed which predicts the effects of feed, corner/nose radius, cutting edge radius, and material on surface generation phenomenon. Unique assumptions are utilized to closely approximate two phenomena of high relevance: side flow and elastic spring back. While limitations exist within this framework, the developed model is found to accurately predict surface roughness in multiple materials and shows the general effects of the varied parameters on near surface material hardness with some confidence.

CHAPTER 2. TECHNICAL BACKGROUND AND PREVIOUS WORK

2.1 Finish Machining Principles

2.1.1 Motivation

Finish machining provides the ability to create surfaces of smooth topography and good resilience to deteriorative phenomena such as wear or fatigue failure. Engineered surface qualities like these are of great importance to industries including aerospace, biomedical, automotive, power generation, etc., which rely upon machined components to perform critical tasks in a cost effective manner. These components are often responsible for bearing various mechanical, thermal, and chemical loads. Prominent examples include bearing surfaces, aircraft engine rotors, and biomedical implants. As technological advances accelerate, machined components are challenged to possess ever-increasing functional performance and longer service life. Furthermore, this task of increasing the machining-induced reliability and functionality (surface integrity) of machined components has been made more difficult by the development of superalloys that are superior in their physical properties to common materials such as steel, aluminum, etc., thus increasing the apparent thermal and mechanical loads on both the workpiece and tooling during manufacturing.

Historically, the topography of machined surfaces has been a key surface integrity specification of manufacturers. It is easily recognized that parts in high precision applications should not only fit well dimensionally, they must mate well tribologically in order to operate efficiently and without excess wear. Thus, creating components with appropriate surface roughness for the given application is paramount in manufacturing. However, investigations into component failure and function have revealed that the machining-affected material properties of this surface - as well as those of the subsurface layers - are of high importance to part performance. At this point it has been well established that the functional performance of machined parts is profoundly tied to the regularity and quality of both the topography and subsurface material properties of the produced surfaces.

A host of manufacturing processes are commonly utilized to produce surfaces of varying precision. Figure 2.1 shows some of the most common processes, as well as the roughness ranges that are achievable for each given process. Within the “mechanical finishes” section, it may be observed that conventional milling and turning operations are generally employed in operations requiring less stringent surface finish standards than finer processes like grinding.



Figure 2.1. Surface roughness produced by common methods (modified from [2] with permission of Elsevier Inc., submission ID 1035201).

While this figure is dated, many of the relative relationships have remained fairly constant throughout manufacturing advances. The precision gap between grinding and processes like milling, turning, and shaping still exists today. Generally, with greater precision, comes greater expense; specialized processes like grinding require additional

equipment and personnel. Due to this, there is considerable drive to utilize relatively inexpensive processes like conventional turning and milling at progressively finer finish specifications. The finishing abilities of these processes are coupled with relatively high material removal rates (MRR) that make them even more desirable from an economic standpoint. Furthermore, it is known that machining processes like turning and milling can be manipulated in such a way to induce subsurface material alterations, which in turn improve the functional performance of the final product. This inherent ability of milling and turning contrasts with grinding, which cannot be manipulated in a similar manner. Inducing similar subsurface material alterations in a ground surface necessitates the use of additional processes like burnishing or shot peening, which adds additional expense to the creation of a given component. However, implementing conventional milling and turning at these fine finishes often leads to undesirable surface characteristics. At the lower extremes of turning and milling's achievable roughness ranges (where the cost and time-saving advantages are most relevant), machining mechanics become unpredictable due to the aforementioned size effects that occur in this regime. In order to more effectively implement conventional finish machining at these fine finishes, further investigation into the fundamental mechanics of surface generation is warranted.

2.1.2 Surface Generation Basics

Finish machining processes on which this work is focused are so called "three-dimensional" processes such as turning, milling, shaping, etc., where the surface of the component being machined is created by multiple adjacent tool cutting edge paths, typically of non-linear nature. Each tool path intersects with the surface created by the previous tool path. These operations create surfaces that are formed primarily by the secondary edge of the tool. On the other hand, two-dimensional processes such as orthogonal turning, broaching, form turning, band-sawing, etc., create surfaces by primary edge only, meaning that the tool's cutting edge never intersects the surface generated by the previous tool path. An example of a surface generated by a turning operation (three-dimensional tool path) and a cross-section of the workpiece/tool geometry is shown in Figure 2.2. Note the intersection of the tool with the previously generated surface in Figure 2.2b.

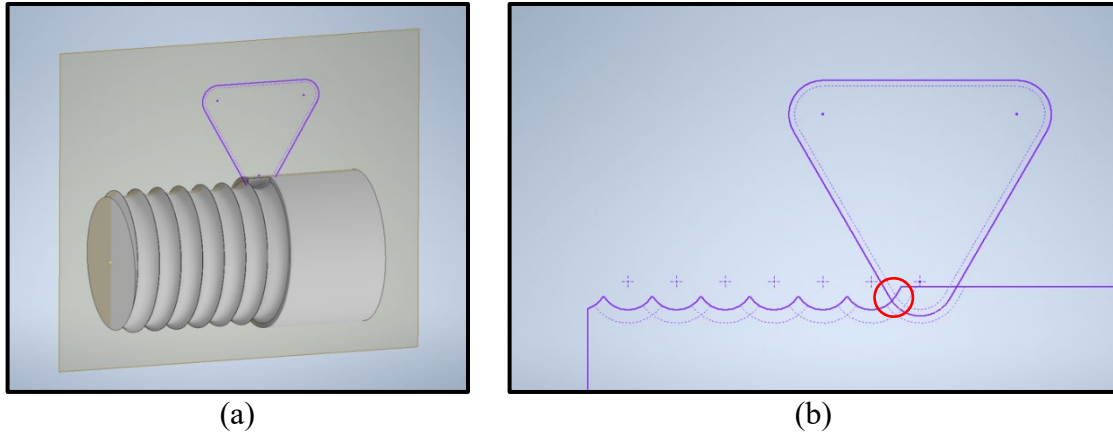


Figure 2.2. (a) Three-dimensional model of basic turning geometry; (b) cross section of the three-dimensional model displayed on the left. Note the presence of affected subsurface area denoted by dashed lines.

2.1.3 Surface Topography

The end goal of finish machining is to produce a surface with characteristics that are within the specified limits for a particular part. Manufacturers often specify surface finish (topographical characteristics) as the only surface integrity specification. One of the most dominant parameters used to assign a standard value to surface topography is the “Arithmetical Mean Height”, denoted by the term R_a . This parameter quantifies the given roughness of a surface by integrating the area between a two-dimensional profile of the surface, and the arithmetic average of the entire profile, as shown in Figure 2.3.

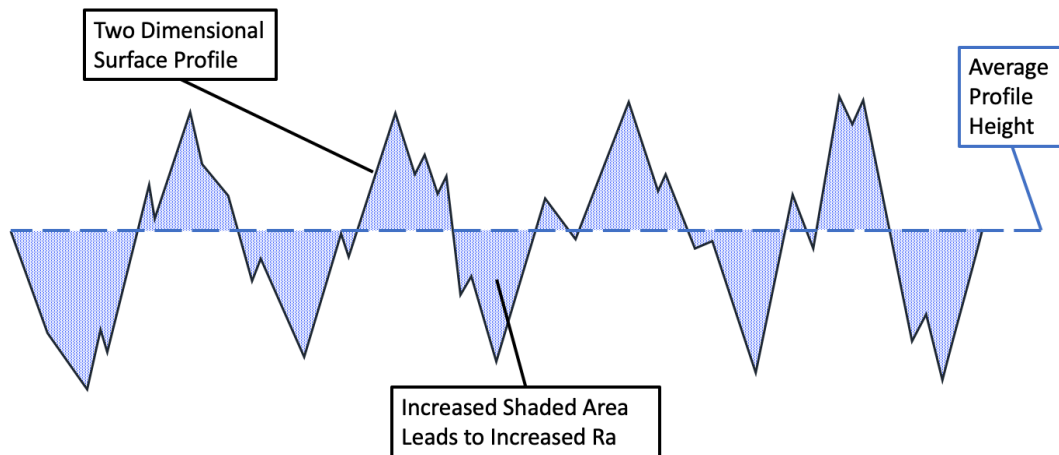


Figure 2.3. Illustration for the calculation of Roughness Average R_a .

Surfaces of finish $R_a < 1 \mu\text{m}$ are frequently called for in finish turning. In general, competent machining of surfaces with this level of roughness requires that certain conditions be met. The relevant conditions of individual processes vary, but the those that typically dominate the determination of surface roughness are generally geometric and vibration-related.

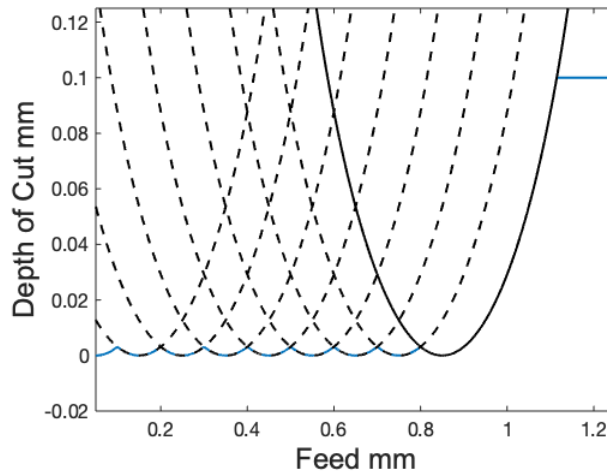


Figure 2.4. Basic turning surface generation geometry showing the replication of the tool corner radius onto the workpiece.

At the most basic level, the turning process is the repeated projection of the tool surface onto a workpiece surface, which may be modeled as shown in Figure 2.4. Since the resulting theoretical surface is geometrically defined, the parameters that influence this geometry may be modified to reduce the perceived roughness. The two parameters affecting the geometry of the surface in the case of turning are feed (the spacing between adjacent tool path segments) and corner radius (the round portion of the tool profile which is responsible for the creation of the entire surface for finishing conditions). A “Kinematic” roughness equation (1), shown below, has been previously developed in order to understand the roughness predicted by only considering these parameters.

$$R_a = \frac{f^2}{32r_c} \quad (1)$$

Where f is feed, and r_c is corner radius. It may be observed that the kinematic roughness R_a predicted by this equation will be small for smaller values of feed, and higher values of nose radius. Therefore, in order to achieve fine finishes, feed should be relatively small, while the parameter corner radius must be relatively large.

Additionally, vibration must be effectively eliminated from the machining process, as significant vibration will immediately create surfaces which possess a rough finish due to the movement of the tool. Chatter (high-impact vibration which induces a significant change in engagement between the tool and workpiece) is commonly caused by the forces arising from chip shearing behavior, machine tool error, tool wear, and tool/workpiece deflection. In order to reduce the forces that cause chatter, common practice is to reduce the tool nose radius, use a sharper/unworn tool, or decrease the depth of engagement of the tool in the workpiece. Stiffer machine, workpiece, and tool geometries are often employed to reduce the susceptibility of vibration prone processes by increasing the natural frequencies of the workpiece/machine tool system.

Other machining variables can affect surface roughness as well. Workpiece material behavior (side flow, cracking, built up edge, pullouts, etc.), coolant/lubricant use, machine tool errors, tool wear, and tool edge roughness are among the most common factors that affect the roughness generated by machining processes. The culmination of all related variables gives way to the induced surface topography. It should be noted that due to all these factors, the kinematic equation is rarely an accurate representation of the final surface roughness, especially in finish machining.

2.1.4 Subsurface Properties

The surfaces imparted by finish machining are often desired to have properties which lead to increased performance and lifetime. The most common method of improving a machined surface in this respect is to eliminate any obvious surface defects such as cracking, excessive plastic flow, discoloring, etc. All such visual features signify a subsurface which has been altered in a way that is deteriorative to the component's performance. However, investigations have shown that significant performance improvements in the material's residual stress, hardness, etc. may be made past the point of no visual damage.

Opposed to roughness phenomena, visual defects do not have easily identifiable geometric relationships to machining parameters. Nevertheless, some qualitative connections are identifiable. Often, visually observed phenomena can be reduced by

ensuring the quality and condition of the machining tool. Very blunt or worn tooling can encourage excessive plastic flow, higher thermal loading, and higher mechanical loading at the tool/workpiece interface. Other machining process parameters such as feed, depth of cut, nose radius, cutting edge radius, tool material, cutting speed, coolant/lubricant type, etc., can also lead to significant change in visual surface defects.

Likewise, non-visual machining-induced surface integrity properties like residual stress, hardness, microstructure alterations, etc., are not easily correlated to specific geometric relationships, perhaps even less so. Generally, favorable mechanical compressive effects can be achieved by enlarging a typical “sharp” tool cutting edge radius slightly. However, this enlarging of the cutting edge may also lead to detrimental thermal effects which can induce thermal softening of the workpiece and yield tensile residual stress due to phase change. Tool wear is typically considered a negative condition in machining, yet in some cases, slight tool wear has been shown to improve the residual stress-state (bias towards compression) of the generated surface. Similar to visually observed defects, non-geometrical factors play a major role in the development of subsurface material properties as well; these factors include material behavior, interfacial friction, tool material, etc. Thus, the problem of predicting subsurface material properties is a complex one.

2.2 Surface Generation and Surface Integrity in Finish Machining

2.2.1 Surface Roughness

It is well understood that size effects begin to dominate the produced surface roughness in the finish machining regime [3]. However, the phenomena that lead to these size effects are difficult to characterize. The most commonly investigated roughness-related size effect is the increased surface roughness caused by the tool cutting edge roughness, however it is clear that this is not the only dominant size effect in finish machining surface generation [4]. The size effects caused by minimum uncut chip thickness and side flow on increasing surface roughness in finish turning have been acknowledged as being significant for some time. However, these two phenomena are not often considered to be related.

Moll [5] was perhaps the first to record the discrepancy between actual and kinematically predicted surface roughness values at low feeds. Sokolowski [6] introduced the premise of a minimum uncut chip thickness (h_{min}), defined formally as the chip thickness required to remove material from the workpiece. The h_{min} effect is now widely recognized as resulting from the finite sharpness of the cutting edge (cutting edge radius, r_e). Albrecht [7] was among the first to demonstrate the relevance of the cutting edge radius to process forces, as well as surface generation. Analytically determining the exact behavior of h_{min} has proven difficult, but it is generally understood to increase with edge radius [8]. Brammertz [9] applied the idea of h_{min} to turning, theorizing that, due to this phenomenon, there must be some part of the uncut chip thickness left on the surface of the workpiece, at the location where the chip thickness approaches zero on the secondary edge; Brammertz famously termed this area of uncut workpiece material the "Spanzipfel". In many subsequent studies, this material is assumed to behave elastically (spring back), which implies significant surface roughness increase at low-feed rate, high-nose radius conditions (i.e., low kinematic roughness) [10, 11]. The kinematic roughness equation was modified by Brammertz [9], as shown in the following equation, to account for the roughness increase caused by the Spanzipfel material left on the machined surface.

$$Brammertz R_t/R_z = \frac{f^2}{8r_c} + \frac{h_{min}}{2} \cdot \left(1 + \frac{h_{min} \cdot r_c}{f^2}\right) \quad (1)$$

where f is feed, r_c is tool nose corner radius, and h_{min} represents the minimum uncut chip thickness. Note that the leftmost term in Equation (1) is the kinematic roughness equation, which predicts the roughness of a surface created by assuming perfect material removal, as shown in Figure 2.5a. While Equation (1) does predict the commonly observed discrepancy in actual and kinematically predicted surface roughness at low-feed rates, studies show that actual roughness values tend to be substantially smaller than those predicted by this equation at low kinematic roughness [12, 13]. Indeed, this discrepancy can be traced back to Brammertz's underlying assumption that any material within the Spanzipfel region will spring back elastically, as indicated in Figure 2.5b. In reality, it is clear that some plastic deformation will occur to the uncut material, which is subject to significant deformation during movement underneath the cutting tool and/or side flow. Shaw and Cookson [14] hypothesized later that the h_{min} material will be plastically

deformed when it is pulled under the tool, and should not account for the roughness discrepancy at small feeds. However, an early (1961), almost forgotten landmark work by Lambert [15] ingeniously demonstrates that the material that is left behind due to Sokolowski's h_{min} effect is not confined to Brammertz's Spanzipfel region. Rather, Lambert found the material under h_{min} is left behind over the entire engaged cutting edge. Therefore, the commonly used surface generation assumptions utilized to arrive at the Brammertz-type models are not valid for workpiece materials responding in a plastic manner (i.e., most metals and plastics).

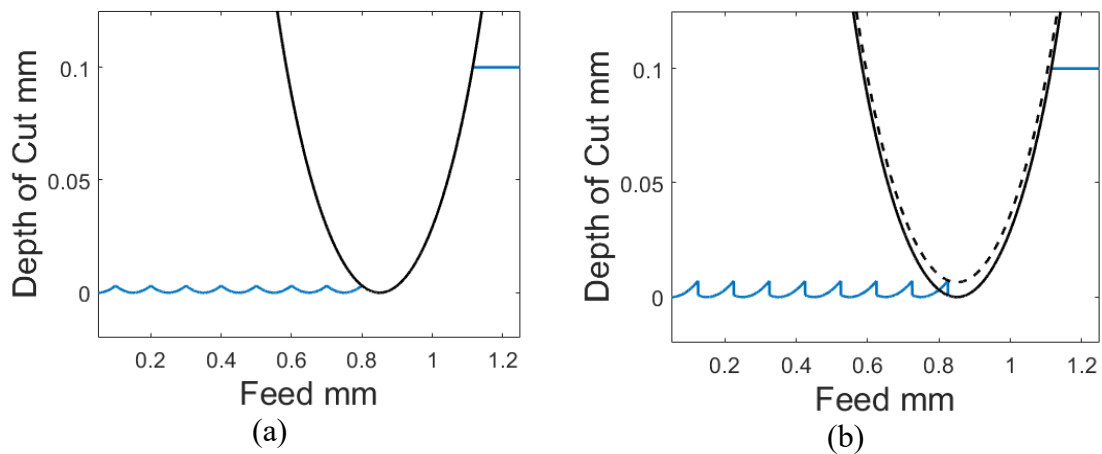


Figure 2.5. (a) Simulated surface from turning, created assuming perfect chip removal; (b) Simulated surface created by assuming material in the Spanzipfel region is left on the surface and behaves elastically. Adapted from author's published work with permission from MDPI [16].

As an alternative cause for increased roughness at small feeds, material side flow (MSF) has been investigated to some extent. Sata [17] investigated MSF's influence on roughness for different materials and found it to be more relevant in the machining of ductile materials. A few studies have noted that observed MSF is responsible for surface roughness deterioration in finish turning [18-21]. Finish turning conditions (high cutting speeds, low feeds and depth of cut) lead to high temperatures at the tool/workpiece interface, causing severe workpiece material plasticization, which then encourages MSF. Typical surface geometry indicative of MSF is shown below in Figure 2.6.

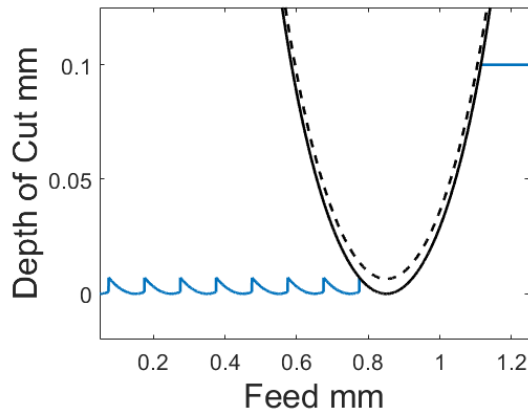


Figure 2.6. Simulated surface created by assuming some constant amount of material is pushed to the side during each tool pass. Adapted from author's published work with permission from MDPI [16].

Kishawy and Elbestawi [22] investigated the MSF phenomenon and noted that roughness was significantly influenced by cutting tool edge preparation, which in turn directly influences the value of h_{min} . However, Kishawy et al. did not include a cutting edge radius parameter when developing the FEA model presented in [21]. Liu and Melkote. [23] developed a model for surface roughness prediction that accounts for side flow in diamond turned surfaces, but considered edge radius to be negligible (a reasonable assumption for single crystal diamond tools at practical feeds). El-Wardany and Elbestawi [19] thoroughly investigated the occurrence of MSF and noted that it was influenced by tool nose radius, feed, tool wear, and h_{min} , mentioning that edge radius has a direct effect on h_{min} , and therefore MSF. Many similar studies look to tool edge surface roughness and tool wear to account for side flow. While these parameters are certainly relevant, little work has sought to define the evident relationship between roughness due to side flow, in light of h_{min} .

More recent contributions in the study of machined roughness have focused some on this relationship. Ozel et al. [24] showed the condition of the edge is a relevant roughness parameter in the hard turning of H13 steel. Ozel and Karpat [25] subsequently demonstrated the effectiveness of an ANN model for predicting roughness within a single dataset. This model considered tool edge geometry on a limited basis. Thiele and Melkote [26] studied edge geometries in hard turning of AISI 52100 steel and concluded that larger tool edge radii increased roughness by ploughing phenomena. Zhao et al. [27] presented a limited investigation on the effect of tool edge radius on surface roughness in AISI 52100

steel. Childs et al. [4, 12] have experimentally investigated the effect of cutting edge radius on surface roughness in finish turning in multiple materials, and found that machine tool error can be a more dominating factor of finish turning roughness on conventional machines. Geometric modeling of surface roughness that accounts for tool edge geometry was performed in [28], but lacks significant validation and makes dubious assumptions. Schultheiss et al. [29] presented an analytical roughness model that takes into account h_{min} , but their definition and determination of h_{min} relies on questionable assumptions. Kountanya [30] developed a three-dimensional model that accounted for tool edge radius and roughness effects, and showed similar trends as previous two-dimensional efforts. Knuefermann [13] developed a geometric model to predict surface roughness based on tool geometry, edge defects and asynchronous error, yet ultimately does not consider side flow effects due to tool edge radius. Furthermore, many recent optimization studies of finish turning do not consider the effect of tool edge radius [31-33]. Hence, the relationship of roughness increase due to side flow (in light of tool edge radius) has been demonstrated to be relevant, yet is not commonly considered in recent works, and requires clarifying.

Roughness models that do consider the effect of h_{min} are often concerned with microcutting or diamond turning, where edge chamfers/radii are so small (on the scale of nanometers, rather than micrometers) they may nearly be neglected at reasonable feeds, as stated in [20]. Zong et al. [34] developed a model to predict roughness in diamond turning and gave consideration to MSF. Chen and Zhao [35] established a roughness prediction model that demonstrated an increase in roughness due to side flow. He et al. [36] has developed a model for diamond turning that incorporates plastic side flow based on a minimum chip thickness value. However, the incorporation of side flow is rather simple and relies upon multiple fitting of constants for calibration. In diamond turning, edge roughness is often a more relevant parameter than the minute value of h_{min} found on diamond tools, yet is not highly relevant in the comparatively duller tooling of precision and conventional machining. Additionally, these previous works have been primarily concerned with mathematically investigating surface roughness phenomena, and generally do not approach the understanding of the geometry of surface generation mechanics.

Little published work exists on the influence of tool edge radius on roughness due to process damping in turning. Alternatively, many studies have studied the evident link

between observed vibration and surface roughness [13, 37, 38]. However, predicting this small-scale vibrational error in industrial applications is not trivial. Chatter prediction has been studied in depth as noted by Altintas and Weck [39]. However, chatter is deemed outside the scope of this work, as it is generally not acceptable in finish machining. Recently, observations were made by Biermann and Baschin [40] in micromilling surfaces regarding improved roughness due to process damping related to tool edge radius. Yusoff et al. [41] remarked that the role of edge geometry was significant in the damping of ‘macroscopic’ milling. Budak and Tunc [42] present an excellent approach to modeling process damping in turning. However, the effort is still primarily concerned with chatter. Generally, previous efforts have not considered tool edge geometry’s effects on small positional errors of the tool that lead to surface roughness increase in very fine finishing.

2.2.2 Subsurface Properties

The study of machined layer subsurface properties is considerably more contemporary than that of surface roughness. One of the foremost recognized studies in this field was conducted by Henriksen [43] in 1951. These efforts served to illuminate the apparent impact of machining processes on the final residual stress state of part surfaces. In addition to recognizing the presence of machining induced residual stresses, Henriksen made the observation that mechanical effects were of greater relevance than thermal stresses in the development of residual stress. Field et al. [44] at Metcut subsequently published a monumental work in 1964 that showed many other meaningful characteristics of a machined surface. They introduced the concept of surface integrity, otherwise known as “SI”. Their work in [45] presents a comprehensive evaluation of surface integrity phenomena that are encountered in the machined surface, including plastic deformation, microhardness, residual stress distribution, etc., and has largely set the stage for subsequent surface integrity analysis efforts. In 1972, Field et al. [2] introduced a table that lists the relevant phenomena an effort should investigate in order to conduct a wholesome review of the surface integrity of a particular parameter set, shown below.

Table 2.1. Different levels of surface integrity data sets for the inspection of machined components (modified from [2] with permission of Elsevier Inc., submission ID 1035201).

Extended Set	Standard Set	Minimum Set	1) Surface Finish (topography)
			2) Macrostructure (10x) or less <ul style="list-style-type: none"> a) Macrocracks b) Macro-etch indications
			3) Microstructure <ul style="list-style-type: none"> a) Microcracks b) Plastic deformation c) Phase transformations d) Intergranular attack e) Pits, tears, laps, protrusions f) Built-up edge g) Melted and redeposited layers h) Selective etching
			4) Microhardness
			5) Fatigue tests (screening)
			6) Stress corrosion tests
			7) Residual Stress and distortion
			8) Fatigue tests (extended to obtain design data)
			9) Additional mechanical tests <ul style="list-style-type: none"> a) Tensile b) Stress rupture c) Creep d) Other specific tests (e.g., bearing performance, sliding friction evaluation, sealing properties of surfaces)

The table is divided into minimum, standard, and extended data sets. Data that is considered mandatory for even the simplest of surface integrity investigations is shown under the minimum data set, which establishes a higher relevance of these parameters in typical machining. Within these sets, certain phenomena are studied with more frequency due to their complexity and relationship to component performance metrics like fatigue life (i.e. residual stress, roughness, cracks, etc.), wear resistance (i.e. hardness, roughness), and friction characteristics (roughness).

Following Field et al.'s fundamental work in [2], Bailey and Jeelani [46, 47] investigated the machining-induced surface integrity, both in terms of altered material properties and metallurgical changes. Liu and Barash [48, 49] subsequently studied the formation of a machined part's surface and subsurface, with regard to both sharp and worn

tools. Griffiths [50] made a major clarification on the occurrence and nature of the often cited near-surface ‘white layer’. The effect of workpiece hardness and other material properties has been investigated by Jeelani et al. in a series of publications [47, 51]. Jeelani et al.’s work within the regime of machining-induced residual stress analysis is of particular importance as it established a relationship to the resulting lifetime of machined parts which undergo fatigue failure. Tönshoff and Brinksmeier [52] published a survey of the relevance of each physical surface integrity property to the failure type of a given machined component. More recently, Griffiths [53] has brought together many aspects of surface integrity measurement, characterization, process parameter relationships and functional performance relationships. This survey verified many of the original results of Tönshoff and Brinksmeier, and added additional context as to the relationships between the subsurface material properties of machined components and the various types of failure. Griffiths modified a table originally published in [52] to summarize the results of this study, shown here as Figure 2.7.

FAILURE CAUSE	SURFACE PHYSICAL PROPERTIES						
	Yield Stress	Hardness	Strength	Fatigue	Residual Stress	Texture	Micro-Cracks
Plastic Deformation	●	●				☆	
Scuffing/adhesion		●					
Fracture/cracking	+	+	●		+		▶
Fatigue				●	▶	▶	●
Cavitation		▶					▶
Wear		●		☆	▶	+	☆
Diffusion						"	
Corrosion					▶	☆	●

Key:

●	Strong influence	} Original 1980 Survey: (Tonshoff and Brinksmeier, 1980)
▶	Traceable influence	
"	Supposed influence	
☆	Additional information (Griffiths, 1988)	
+	Additional information (Griffiths, 2000)	

Figure 2.7. Chart of material properties that are relevant to failure types. (reproduced from [53] with permission of Elsevier Books Limited, reference number 40346, originally modified from [52], with permission of Elsevier Inc., license number 4875501237893).

It is therefore well understood that surface integrity is in large part due to machining operations, and that these induced properties have significant impacts on the lifetime of a machined component. However, the genesis of many surface integrity phenomena are still contested, with researchers often publishing conflicting results [54]. Ulutan [55] has shown that the effects of basic cutting parameters such as feed, cutting speed, and depth of cut on residual stress, strain hardening, and surface finish are still not well understood in the machining of Titanium and Nickel-based alloys. This implies that there is some other factor in surface generation that requires clarification. This missing factor is most likely edge geometry, and is mentioned in [55] as relevant to surface integrity, but has yet to be investigated as thoroughly as the other factors mentioned. Many relevant surface integrity threats arise due to the plastic deformation of material on the machined surface, which is highly influenced by the characteristics of the cutting edge geometry of a particular tool. This material is highly strained and results in a temperature increase, leading to mechanical effects from the apparent strain, and thermal softening of the surface due to the temperature increase. These deformations can be affected by a range of factors including cutting parameters, workpiece material properties, tool geometry and material properties.

2.2.2.1 Hardness

One of the earliest investigations into machining-induced microhardness and residual stress was that of Tondshoff and Brinksmeier. They have advised that the induced microhardness change seen in machining is relevant when considering failure due to plastic deformation, scuffing/adhesion, cavitation, and wear [52]. Griffiths and Furze [56] proved that the presence of a strain-hardened subsurface layer will lead to increased wear resistance. Surface hardness can also easily be five times the value of the bulk hardness, making a load bearing surface which is very brittle, and prone to failure [53]. Ground surfaces investigated in [52] showed that a tempered (thermally softened) layer extended further into the subsurface when the grit size was decreased, corresponding to an increase in thermal loading and a decrease in mechanical loading. This effect is easily observed in Figure 2.8, reproduced here from the same study.

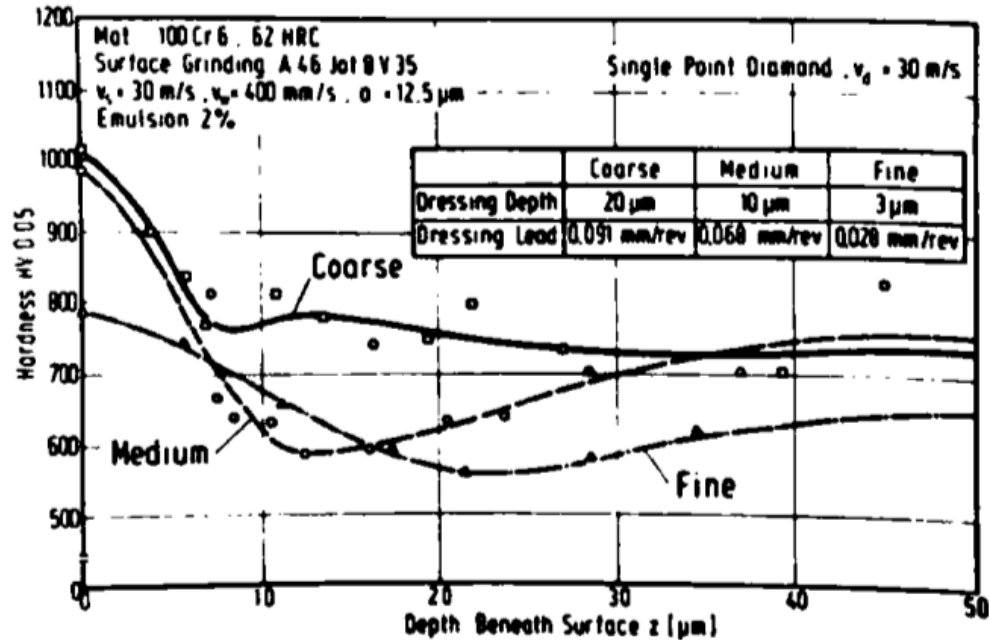


Figure 2.8. The effect of dressing conditions on observed microhardness induced by grinding (reproduced from [52] with permission of Elsevier Inc., license number 4875501237893).

Given a lack of microstructural change like grain refinement, twinning, or phase change, relative hardness of a material will generally decrease under tensile residual stress and increase under compressive stresses [57]. This further signifies the relevant use of microhardness to evaluate surface integrity. While some publications [58] have disagreed with the notion that optically observed indents (i.e. Vickers hardness tests) can capture residual stress behavior, the general consensus is that hardness in general has some correlation to increased residual stress, outside of microstructural changes. Hardness values derived from load/displacement tests (rather than optical) are typically recognized as more sensitive to residual stress. Lee [59] has shown that residual stress appears to have an approximately linear relationship with hardness increase when a bulk sample is placed under tensile and compressive loadings. Griffiths [53] has noted that generally, the depth of machining-induced residual stress penetration is usually on the order of tenths of millimeters, while measurable hardness alteration penetration depth is usually some fraction of the depth of residual stress. While hardness values may be used to qualitatively assess residual stress characteristics, care must be taken to recognize any major metallurgical changes which may lead to an observed increase in hardness, which does not

reflect a similar increase in compressive stress state. For example, a phase change due to thermally abusive conditions may lead to an increase in the observed hardness, while the residual stress state remains the same or is in fact made tensile by the phase change.

It is possible to achieve enhanced surface integrity by using tools with rounded or chamfered cutting edges which induce compressive layers, without subjecting the workpiece surface to undue thermal stresses. Griffiths [60] noted that a tool with a burnishing wear land would create surfaces of increased surface integrity. Wardany [61] found that microhardness change was not observed more than 55 μm below the machined surface at feeds and speeds within the finishing regime in the machining of tool steel. More heavily worn tools were found to cause a slight softening of material below the surface, and a hardening effect near the surface, while sharper tools exhibited the opposite effect [61]. However, Wardany did not remark on any significant correlation between the tool macro and micro geometries' role in the development of strain hardened material.

While many studies have considered hardness as a function of depth below the machined surface, few, (if any) studies have pointed out the potential for material property variation in the direction of feed (perpendicular to both tool path and depth of cut direction). This is most likely due to the time and resolution required to achieve such data, however, nanoindentation (a relatively new method) is capable of easily generating this data. Nanoindentation has recently been applied to mapping the material property characteristics of a 2D section of material in polymers [62], however, this technique has yet to be explored in machined subsurfaces. Warren and Guo [63] have investigated the use of nanoindentation only to observe properties as a function of depth from the machined surface. They noted that in addition to estimation of hardness and material modulus, residual stress could be qualitatively predicted by the method.

2.3 Closing Statements

This literature review therefore makes clear that machining has been shown to have great impact on the surface integrity of machined surfaces. Many machining parameters have been previously revealed to be relevant to both topographical and subsurface phenomena. However, in spite of all previous work in studying and predicting machining-

induced surface integrity in two dimensions, relatively little work has been done to understand and predict the development of surface integrity in three dimensions. Generally, in order to induce increased surface integrity in ductile materials (i.e., desired material properties like compressive residual stress depth, increased hardness, etc.), a larger tool cutting edge radius may be utilized. However, in three-dimensional machining processes this may lead to other undesirable affects such as increased roughness due to side flow, higher cutting forces, higher cutting temperatures, etc. An appropriate balance between all relevant surface integrity parameters must be found. Acknowledging this gap in literature, this thesis seeks to illuminate some aspects of surface integrity development in the surface generation of 3D machining processes such as turning and milling. While the scope of the presented work does not encompass all concerns and parameters that affect surface integrity, parameters relevant to the expansion of surface integrity prediction to three dimensions are considered.

CHAPTER 3. EQUIPMENT AND PROCEDURES

3.1 Finish Turning

Experimental work to illuminate relationships between process geometry and surface generation was conducted by means of face turning trials on a HAAS TL2 CNC lathe, as shown in Figure 3.1. Modified Kennametal TPGN (triangle) geometries of the uncoated, fine-grained carbide grade K-68 were used. The workpiece material was a cylindrical bar of Ti-6Al-4V (60 mm diameter, annealed condition, 35 HRC).

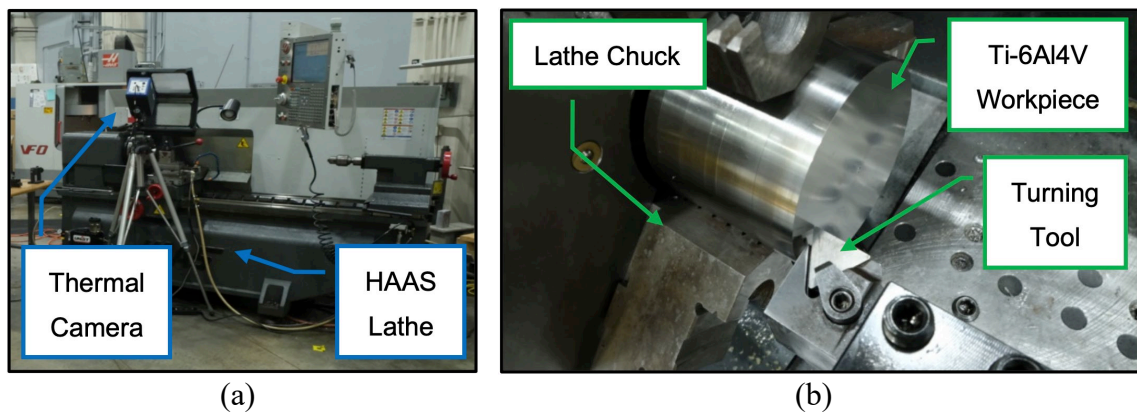


Figure 3.1. (a) HAAS TL2 CNC lathe used to perform cutting tests; (b) Kennametal TPGN K-68 tool of $r_c = 0.8$ mm tool being touched off the Ti-6Al-4V workpiece. Adapted from author's published work with permission from MDPI [16].

A range of feeds and nose radii, outlined in Table 1 below, was selected to provide various combinations of uncut chip geometry and kinematic roughness. Beyond this table, differing conditions of nose radius and feed will be merged and often referred to as one factor: predicted kinematic roughness R_t/R_z and R_a , the equations for which are shown below. All other variable parameters were held constant during these trials. Constant parameters of some consequence include cutting speed (v_c), held at 288 m/min, depth of cut (a_p), held at 0.25 mm, and coolant/lubrication, which was not present.

$$R_t/R_z = \frac{f^2}{8r_c} \quad (2)$$

$$R_a = \frac{f^2}{32r_c} \quad (3)$$

Table 3.1. Experimental Parameters and Levels.

Feed	Nose Radius r_c	Predicted Kinematic Roughness R_r/R_z	Edge Radius r_e
0.1 mm	3.2 mm	0.39 μm	12.5 μm
0.1 mm	0.8 mm	1.56 μm	20 μm
0.1 mm	0.4 mm	3.13 μm	30 μm
0.2 mm	0.8 mm	6.25 μm	
0.2 mm	0.4 mm	12.5 μm	

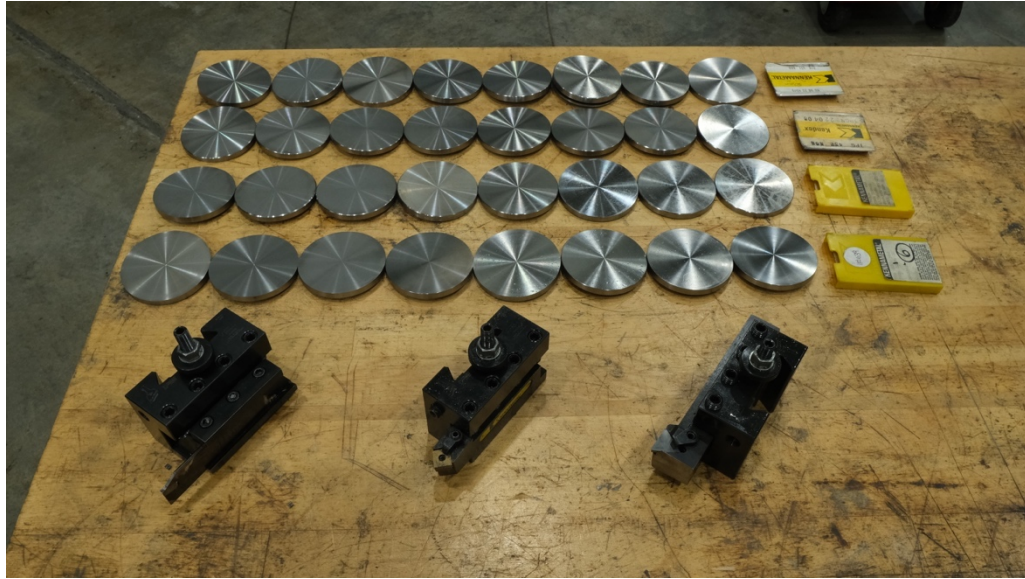


Figure 3.2. The three turning tool types used, and the face turned samples.

Certain precautions were taken in the machining and parting of sample pieces. As can be noted from Figure 3.1, the stick-out of the toolholder and the length of the workpiece stickout from the chuck was kept to a minimum. This led to surfaces that were affected minimally by angular misalignment of the spindle, vibrations due to workpiece center of mass misalignment, deflections due to lever actions of forces on the workpiece, etc. Before each condition, a workpiece cleanup routine was followed which involved the facing of the to-be machined surface with a sharp tool (to eliminate surface irregularities left by the parting process), the chamfering of the exterior edge, and the cleaning of the entire workpiece with a solvent to eliminate any coolant residue that may have affected the following surface generation test condition. The parting off of each sample was a delicate process prone to tool breakage, therefore flood coolant was used to alleviate tool wear progression and the heating of the workpiece. The part-off width of the samples was kept thick at 6 mm in order to protect the samples against alteration of material properties by the potential intense heat and mechanical stress from the parting process.

3.1.1 Cutting Edge Honing

As it has been established that the cutting edge geometry has a significant effect on surface generation in finish machining, a number of carbide cutting tool edges were modified to precise values in order to investigate their effects on surface integrity. The preparation of experimental cutting tool edges was accomplished by a novel honing method that creates tool edge radii with final geometry accuracy variance of less than 20%. This method relies upon the use of a HAAS VF-2 CNC milling machine equipped with a diamond-paste impregnated buffing wheel, shown in Figure 3.3b. In order to generate a moderately repeatable process, an adjustable program was designed in AutoCAD Inventor 2019, the toolpath of which is shown in Figure 3.3a.

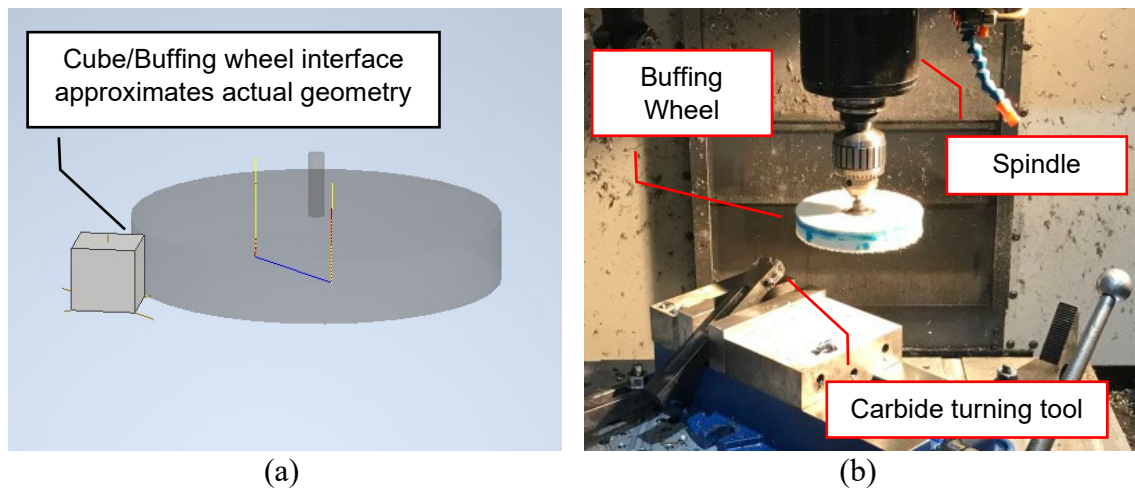


Figure 3.3. (a) Image of the tooling and workpiece geometry created for the tool honing program; (b) CNC milling machine interior, equipped with buffing wheel impregnated with $1\ \mu\text{m}$ diamond paste, carbide turning tool is held in place by a tool and vise.

An example of the tool edge radii generated by this methodology is shown in Figure 3.4. The tools honed by this method exhibit very low edge roughness due to the high-nap nature of the buffing wheel and the small size of the abrasive.

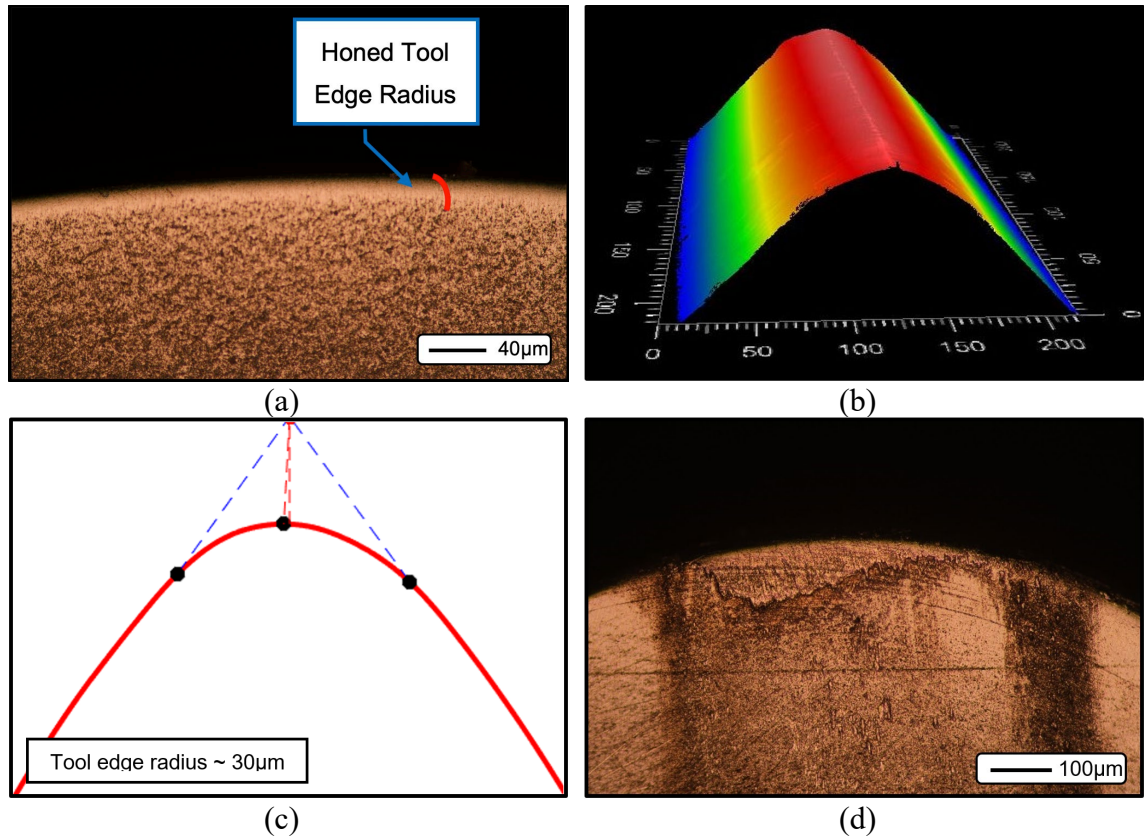


Figure 3.4. (a) Rake face view of modified edge of a Kennametal TPGN K-68 tool of $r_c = 3.2$ mm, $r_e = 30$ μm ; (b); Tool cloudmap produced via scanning white light interferometer; (c) Subsequent analysis of tool cloudmap via MATLAB; (d) Used tool exhibiting tool/workpiece contact discoloration and limited adhesion, but no tool- (edge- or nose-) wear. Adapted from author's published work with permission from MDPI [16].

Throughout the honing of each tool, white light interferometer-generated pointcloud maps representing the honed geometry were created, and each edge was verified to be precise in this way. Some variation is encountered between each individual edge, and the edges were not always found to be of perfect radial geometry (as can be noticed in Figure 3.4c. Nonetheless, each edge was found to be fairly near the desired geometry, with radius values within 20% of the nominal value for each condition.

3.2 Sample Characterization

Characterization methods of the generated samples fall into two categories, topographical analysis and subsurface analysis. The preparation of samples for topographical analysis is fairly simple, as the surface produced by machining is being evaluated directly. Generally, cleaning with a solvent is adequate preparation for common

topographical analysis. On the other hand, preparation of samples for subsurface analysis is more involved, as well as more difficult to convey. In order to ensure understanding of the subsequently presented preparation, analysis, and data, visual aids of the sample preparation process are presented in Figure 3.5. Topographical analysis is performed immediately after the sample piece is created in Figure 3.5b, while subsurface analysis requires the additional preparation processes shown in Figure 3.5d and e. Examples of obtained topographical data and subsurface data are shown in Figure 3.5c and d, respectively.

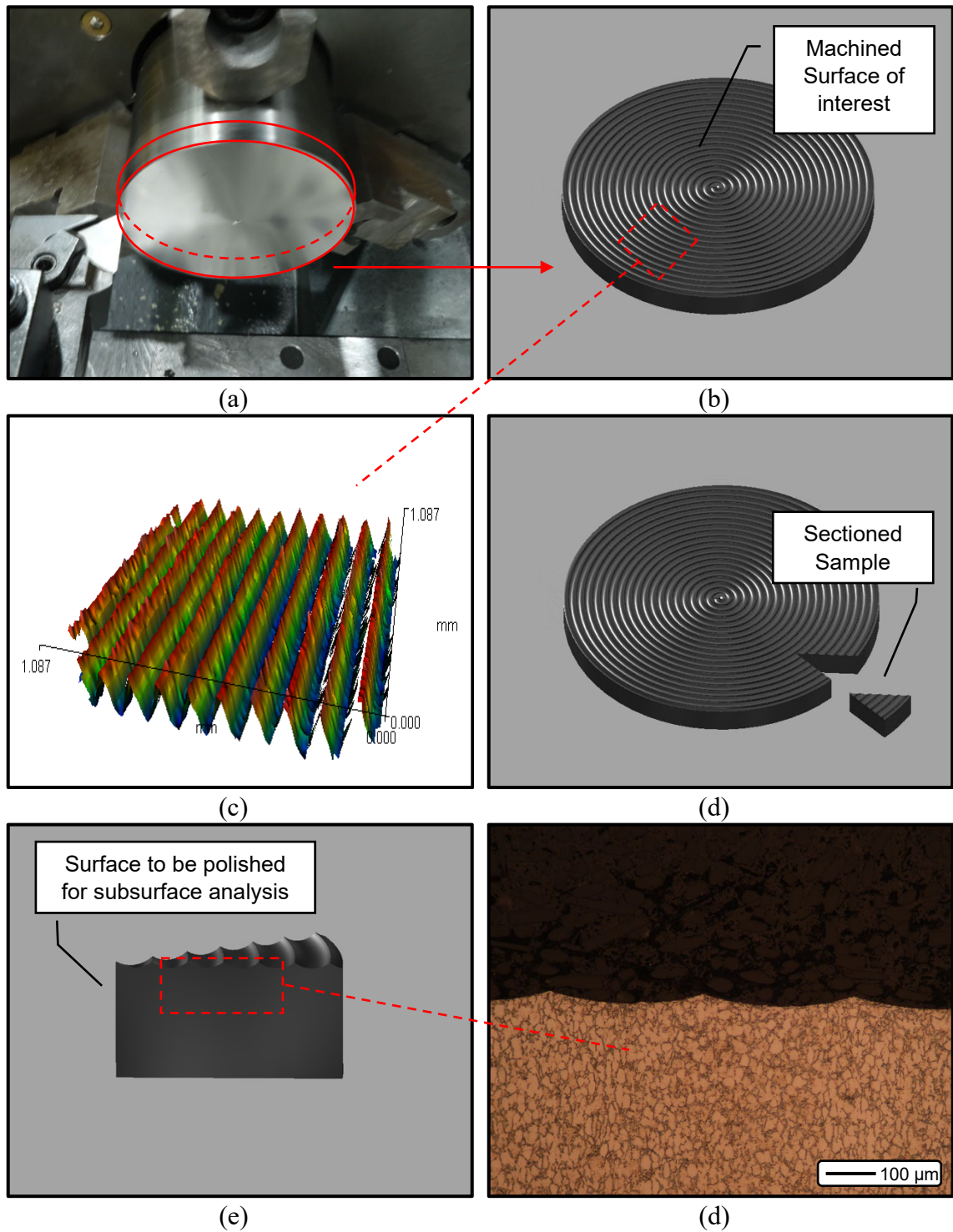





Figure 3.5. Metallographic sample analysis geometry clarification.

3.2.1 Sample Cross Section Preparation

After sectioning an appropriate piece of the sample from the bulk sample, similar to that shown in Figure 3.5d, the surface of interest is of a rough, saw-cut topography. To view the microstructure and perform accurate materials analysis of the subsurface, this surface is then polished to a fine finish. A Struers Rotopol-22 automatic polisher was utilized to polish the samples to this fine finish. The regimen of pads and abrasives used in conjunction with the machine are listed here.

Table 3.2. Polishing Regimen

Step	Pad Type	Lubricant/Abrasive	Force/Specimen	Time	Result
Plane Grinding	220-grit Silicon Carbide	Water	30 N	Till Plane	
Fine Grinding	Low-Nap Woven Nylon	9 μm Diamond Suspension	30 N	5 min	
Polishing	High-Nap Chemical-Resistant Cloth	70% 0.05 μm Colloidal Silica / 30% H ₂ O ₂	30 N	10 min	

The results of this polishing were verified to be of high quality by viewing with polarized light. Samples were considered to be well polished upon the visibility of individual grains. This method eliminates the possibility of obtaining a polish with a heavily mechanically deformed surface layer. An example of a highly polished sample viewed under polarized light is shown in Figure 3.6a.

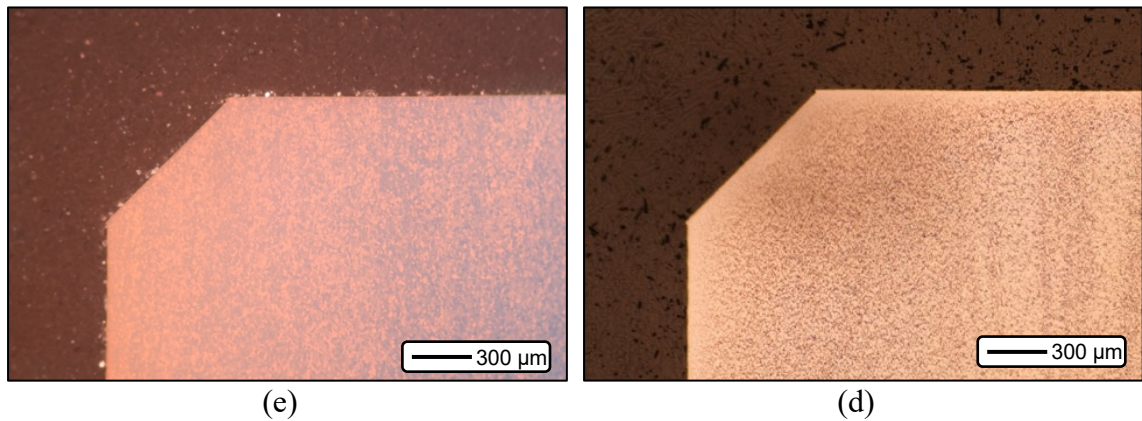


Figure 3.6. Typical results of polishing, (a) viewed optically with polarized light; (b) viewed optically after etching.

The polished samples were also chemically etched to enable clearer view of the material microstructure in optical analysis, as well as to enable the more accurate gathering of data in microhardness evaluation. Details of the etchant process are listed in the following table, and an example of sample microstructure post-etching is shown in Figure 3.6b.

Table 3.3. Kroll's Reagent Use

Recipe	Precautions	Method	Time
6 ml HF + 3 ml Nitric Acid + 91 ml Water	Appropriate PPE and Fume Hood	Swab	10-15s

Upon closer inspection it was found that the images yielded by etching gave an end result which was much clearer at higher magnifications. The viewing of samples with polarized light was then mostly utilized as a polish-checking tool. A comparison of the image quality of each microstructure-exposing method is displayed in Figure 3.7.

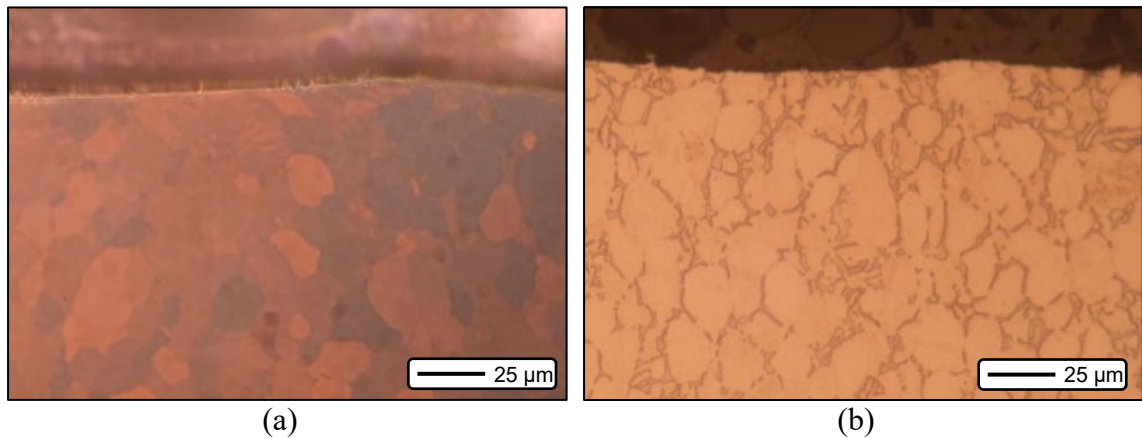


Figure 3.7. Comparison of two grain-viewing methods: (a) polarized light; (b) etching with Kroll's Reagent.

3.2.2 Scanning White Light Interferometry

A Zygo NewView 7300 scanning white light interferometer with a spatial resolution of approximately 2 nm was utilized throughout the experimental work. Initially, this equipment was used to verify the edge geometry of individual tools during honing, as mentioned above. Once each sample had been turned, roughness measurements were taken at multiple locations to determine an average surface roughness value for each surface. The extreme spatial resolution of this tool was also utilized in the verification of various other geometries that were integral to the surface integrity inspection that is described in this text. Geometries of particular importance that were checked on this instrument include the roughness of the polished sample surface, the amount of edge rounding on the polished samples, and the condition of the Vickers hardness tester. Each of these properties was verified at the beginning of study, and multiple times throughout the data collection process to ensure accuracy of results.

3.2.3 Electron and Focused Ion Beam Microscopy

A Helios NanoLab DualBeam 600 was utilized to observe near-surface material alterations within the machined samples. The focused ion beam (FIB) was utilized extensively in order to remove material from the mechanically polished surface. The use of this methodology allowed for the viewing of the near surface structure in a near virgin

state, not readily achievable by mechanical polishing and SEM viewing. A “skimming” method of revealing the near-surface microstructure was developed. This method proved more efficient and reliable relative to the typical “trenching” method usually employed in the viewing of near surface material structures.

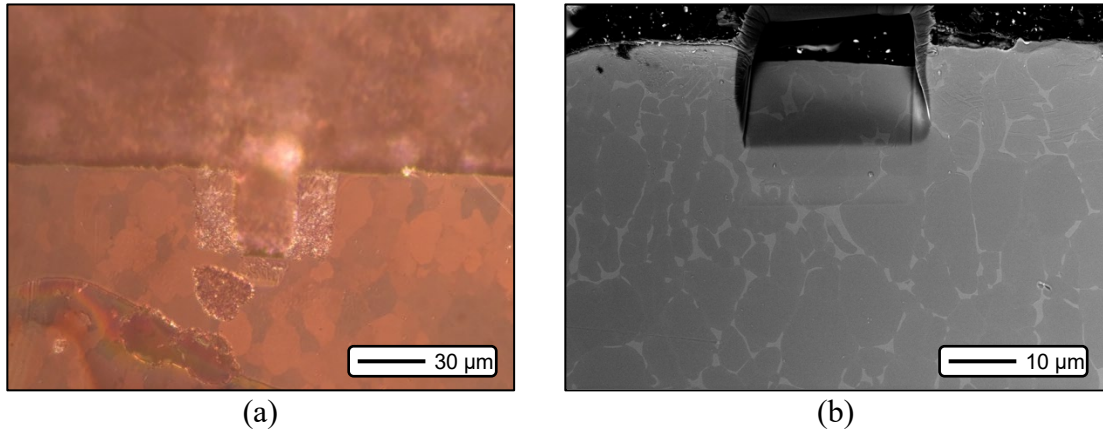


Figure 3.8. (a) Optical image of the geometry produced by the FIB “skimming” method of revealing the near surface microstructure; (b) SEM micrograph showing the resulting skimmed material in better definition.

A custom sample holder was machined from aluminum to improve sample imaging in the SEM by stabilizing the sample both mechanically and electronically, by reducing charge buildup. The sample holder utilized set screws in addition to carbon tape to give maximum mechanical and electronic stabilization.

3.2.4 Optical Microscopy

While some images of sample subsurface characteristics were recorded using SEM, optical methods were the most often used investigation method in the characterization of the subsurface. A FUJI TX-2 camera was used in combination with a Nikon EPIPHOT 300 metallographic optical microscope. The optical objectives used during this examination were 2.5x, 5x, 10x, 20x, and 50x objectives. This microscope was equipped standard with provisions for an array of different techniques. The most commonly used microscope special functions were darkfield lighting, polarized light filters, and Nomarski filters. Darkfield and Nomarski methods were used primarily to highlight the surface roughness of the polished samples, i.e. to check for surface imperfections while polishing. Polarized light was utilized solely to check the quality of the polish, i.e., to establish whether the

polishing process had induced an undesirable plastic deformation layer on the sample surface, rather than expose a nearly untouched material microstructure.

3.2.5 Microhardness Evaluation

Microhardness evaluation of the near surface material was carried out on a Future Tech Group FM7 microhardness tester. A Vickers-type indenter was used for all microhardness testing. Indentations were made on mounted and polished sections of material cut perpendicular to the machining tool path. Hardness profiles of each surface were generated. Typical hardness testing (HRC, etc.) was not conducted as this study is primarily focused on the near surface characteristics which cannot be evaluated effectively by typical ‘macro’ hardness testers such as HRC.

Hardness indents of any kind are affected by the support (or lack thereof) of the surrounding material matrix. In the case of indents made near the edge of the sectioned and polished sample material (as is the case of this study), care must be taken in order to indent in a manner in which the size of the indent is not dependent on the proximity of the sample edge. It follows that larger indents must be placed further to the interior of the sample, while smaller indents may be made closer to the area of interest. Common practice is to place the indent at least 2.5 times its diagonal length away from the sample edge, unless this edge is supported by a material of a similar modulus. Therefore, in order to enable the hardness testing of material very close to the edge, the lowest possible Vickers indent force was selected, 10 gf. The function of microhardness machines is subject to some variability (especially at forces as low as this), so the function of this machine was repeatedly checked. White light interferometer-generated pointcloud maps of the indenter geometry showed no wear at the beginning or end of trials, and calibration blocks were repeatedly used to test the relative accuracy of the microindenter.

Initially, samples were mechanically polished to an extremely fine finish, one which showed no defects, and which was capable of showing grains under polarized light. It was found, however, that indentation of these surfaces led to values of high variability, even for a polished surface of impeccable quality. To address this, the samples were checked and further polished, however these finer samples yielded similar results. Multiple

causes were investigated for this phenomenon. Of all factors examined, grain size and indent placement (relative to grain boundaries) were found to have the most significant effect on hardness variability at a given depth. To showcase this variability, two indents of exact same depth are shown in Figure 3.9. In procuring a hardness profile, it is expected that these two values should generally be about the same, however, the indent placed in the larger grain is about 40 HV lower than the indent placed in the smaller grain. Therefore, to obtain results that would be most relevant to this study, Kroll's Reagent was used to preliminarily expose the grain boundaries. Upon etching, indents could be accurately placed within a single grain of average size, away from grain boundaries. Similar revelations have been observed in [52].

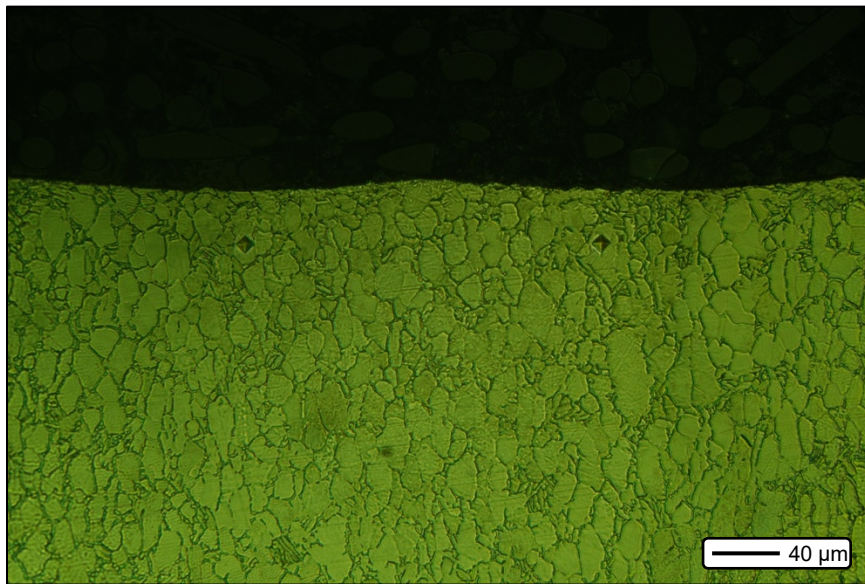


Figure 3.9. Microhardness indents created by a Vickers indenter. One indent is placed within a large grain. The left indent, placed in an average grain of $\sim 10 \mu\text{m}$ diameter, gave a hardness value of 297.1 HV, while the right indent gave a value of 262.2 HV.

3.2.6 Nanoindentation

Nanoindentation of multiple samples was performed with a Nanomechanics (now KLA-Tencor) iNano nanoindenter. This tool utilized a Berkovich-type indenter, controlled by a leadscrew-driven, servo-actuated system. Displacements are quantified on the level of angstroms and force is measured in milli-Newtons; hence extremely precise measurement is possible with this method. Grids of 4 by 10 indents (spaced $30 \mu\text{m}$ apart) were implemented near the surface. An example of an array of indents is shown in Figure 3.10.

Hardness values were extracted from the data collected during each indent (load, indenter displacement, and time), and hardness contour maps were constructed and imposed on the sample section geometry. This automatic instrument enabled the viewing of the subsurface property structure and gave qualitative insight into the residual stress state and strain hardening left in the final surfaces of the machined samples on a two-dimensional level.

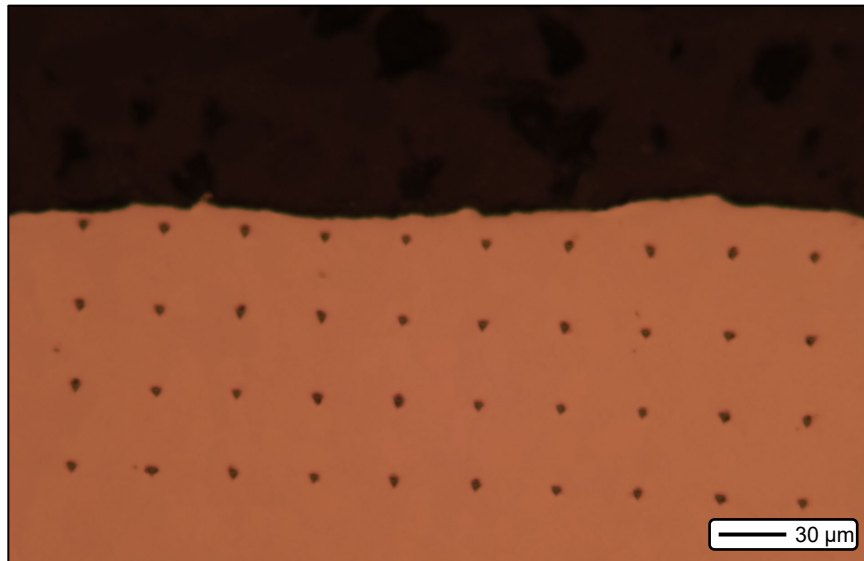


Figure 3.10. Example of nanoindent matrix on a metallographically polished sample, representative of the indentation matrices performed on all investigated samples.

3.3 Model Development

The surface generation model was developed on a Dell Precision 3630 Desktop, with an Intel i9-9900 CPU. 40GB of random access memory (RAM) was utilized as well. Due to these performance-enhancing attributes, the developed model was easily developed and debugged. The model was developed in MATLAB, version 2019b. All functions and logic outside the basic MATLAB-supplied functions were developed in-house. No toolboxes or third party functions were used in any part of development.

CHAPTER 4. SURFACE GENERATION MODEL DEVELOPMENT

4.1 Assumption Development

In order to develop an accurate surface generation model, appropriate assumptions must be made. One key assumption that was incorporated relates to the behavior of material of the uncut chip along the cutting edge under h_{min} , i.e., the Spanzipfel region. Indeed, much of the current understanding is based on Brammertz's Spanzipfel assumption, where material of chip thickness below h_{min} flows underneath the tool, while material of chip thickness above h_{min} is evacuated entirely from the workpiece [10, 11, 64-66]. This represents an on/off transition between ploughing and cutting, and in turn implies the creation of a perfect copy of the tool profile on the workpiece for all points along the tool edge where material is above h_{min} . These assumptions give rise to the pointed Spanzipfel region of material (as can be seen in Figure 2.5b), which is not generally observed on real machined surfaces. In order to realize more accurate modeling of surface roughness, it is imperative to (at least qualitatively) match the model mechanics to the actual physics of the cutting process. This includes the fact that some material does indeed flow under the tool, with spring back subsequently occurring along the flank/clearance face of the tool, as well as the occurrence of side flow of some magnitude—both phenomena having been qualitatively established by Lambert [15].

Arcona and Dow [67] have calculated the spring back of machined material to be a linear function of the tool edge radius for a given material, which follows logically from the h_{min} and conservation of volume considerations. However, in reality this proves to be a simplification of the matter. More experimental understanding of the effect of material properties and tool parameters on the size of this spring back is required for full understanding of its nature [8, 68, 69]. At this point, it seems clear that material less than the h_{min} flows and is deformed under the cutting edge, to be recovered after the tool passes over it. This recovery is often assumed to be largely due to the elastic properties of the bulk material. However, much of the material near the surface is plastically deformed as well, due to ploughing and shear deformation, as illustrated by Oxley and Challen's [70] foundational work on the nature of polishing and wear mechanisms. Nevertheless, the work

presented here shall assume that full spring back will occur for any section of the tool edge where material in this region is well supported from either side to prevent side flow, i.e., where plane strain may be assumed.

Material at the two extreme ends of the uncut chip region, i.e., near the free surfaces of the cut on the primary and the secondary cutting edges, is not under plane strain constraint, and will therefore be susceptible to being “squeezed” out sideways from in between the flank and workpiece, as mentioned in Pekelharing and Gieszen’s work [18]. As a result, the hypothetical Spanzipfel region, which is located at the extreme (secondary) edge of the uncut chip region, does not form. Rather, some material in this region is displaced sideways by the advancing tool edge, due to the high stresses and lack of plane stress. In the presented model, it is assumed that the amount of material which is displaced as side flow is directly related to the geometric area of the Spanzipfel.

These assumptions lead to a side flow region which is dependent upon feed, nose radius, and edge radius, as well as a raised part surface that is established by the elastic spring back of h_{min} . Notably, side flow occurs due to h_{min} in a similar manner as the Brammertz effect is assumed to occur. However, the occurrence and transition between flow underneath the tool (not technically the Brammertz effect, but ploughing/severe plastic deformation akin to the mechanics of polishing and burnishing) and side flow is affected by the ‘boundary conditions’ of the deformation (i.e., presence or absence of rigid material constraints due to adjacent material in the uncut chip), as stated previously.

4.2 Surface Roughness Simulation of Surfaces Generated by Lambert-Inspired Assumptions

The proposed iterative geometric model (code shown in the appendix) initializes by assuming some starting workpiece surface geometry after a single workpiece revolution, as shown below in Figure 4.1a. Any tool geometry and feed may be defined for this model. However, to clearly represent the process in the following figures, the following parameters have been selected: $r_c = 0.4$ mm, $h_{min} = 6.5$ μ m, and $f = 0.1$ mm.

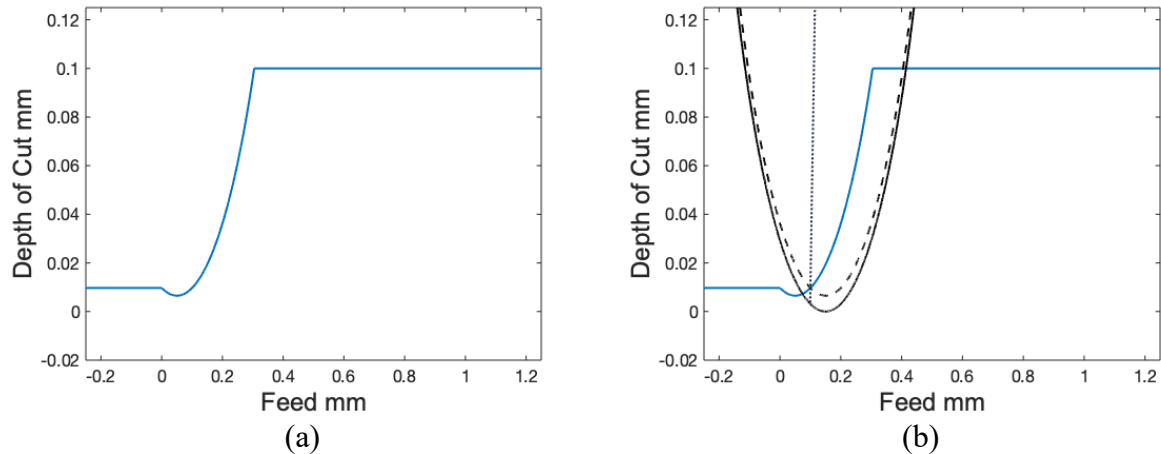


Figure 4.1. (a) Initial model workpiece geometry; (b) Tool geometry imposed on the previously defined workpiece geometry. Adapted from author's published work with permission from MDPI [16].

The curved region in the middle of Figure 4.1a is the ideal tool projection copied onto the workpiece surface, offset to the interior by h_{min} to account for the assumption that the material less than h_{min} will recover on the other side of the tool. It should be noted that the curved section in this and subsequent figures is represented as a circle in the model, yet appears to be elliptical here due to the scaling differential of the x and y axes. The lower linear region is somewhat arbitrary, but it is included as an initial condition necessary to simplify the computation of future iterations. The height of this linear region is again, arbitrary, but set equal to the value of kinematically predicted roughness R_t/R_z in order to approximate the geometry of any previously generated surface. The upper linear region is the existing material surface, to be machined. This will move vertically relative to the other geometry depending on the depth of cut.

Once initial surface geometry has been created, the tool geometry is imposed on the workpiece geometry for the upcoming tool path segment, as shown in Figure 4.1b. The tool geometry is composed of two profiles, shown here as solid black and dashed black. The exterior solid profile represents the true tool profile, while the interior dashed profile represents the tool profile shape, offset by h_{min} . A profile has been added to this image to show where the uncut chip thickness drops below h_{min} , creating the Spanzipfel geometry discussed previously. The plane stress region which occurs at the opposing end of the uncut

chip (on the primary edge) is not typically considered relevant to the final surface geometry, and therefore is not considered in this model.

In order to model the surface profile created by this new tool path segment, this Spanziffl region is then transposed into the open space between the workpiece and tool, as shown in Figure 4.2. A transition surface profile is computed that begins at the peak of this transposed MSF area and gradually approaches the dashed h_{min} profile. This profile is formulated so that volume is conserved in this region, accounting for the displaced side flow volume. Once this profile reaches h_{min} , the newly generated surface will be found at the h_{min} profile (dashed black) over the remainder of the tool edge, not the full tool profile (solid black).

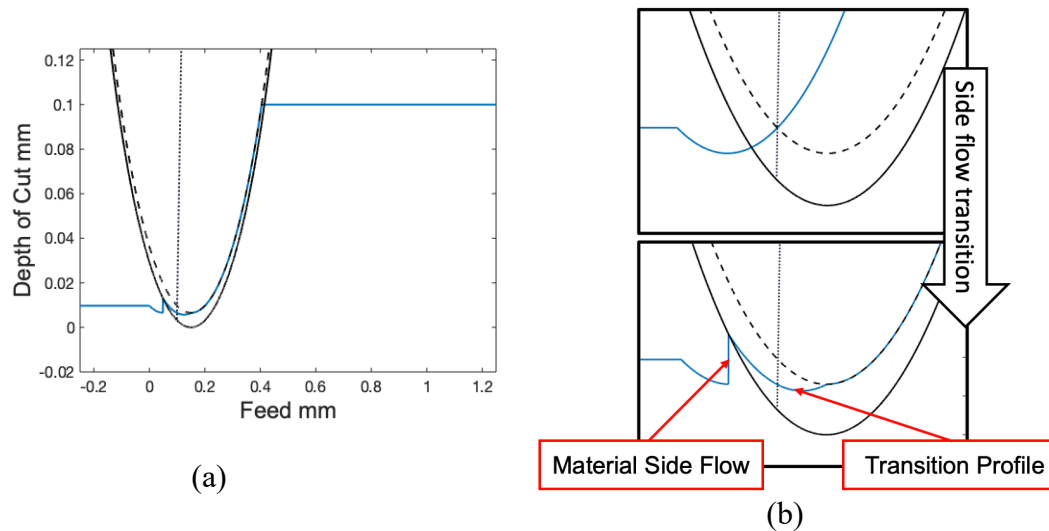


Figure 4.2. (a) Tool geometry imposed on new surface profile, altered by the current tool pass; (b) Magnified examples of the model geometry that clarify the side flow transition and surface profile construction. Adapted from author's published work with permission from MDPI [16].

These profiles are then consolidated to form the new surface profile, and the tool geometry is translated by the feed to begin this process for the next path, shown in Figure 4.3a. This iterative process is repeated until the altered surface profile reaches an adequate length and equilibrium is established, as shown below in Figure 4.3b. This figure also shows the ramifications of the assumption that material spring back will alter the surface profiles generated by the model, as can be seen in the workpiece model's final surface being substantially higher than the tool nose minima at all points.

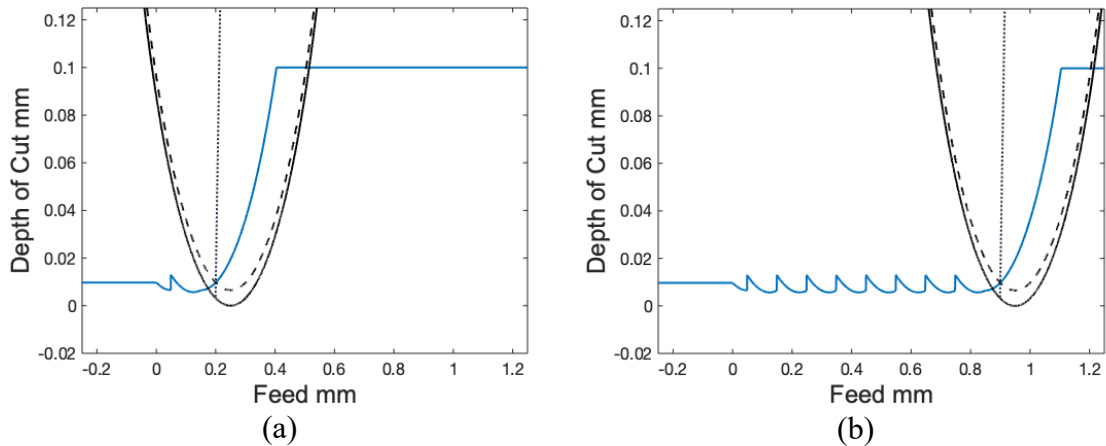


Figure 4.3. (a) Tool geometry in new pass position imposed on the surface profile generated by the previous pass; (b) Surface profile created by the iterative model, shown at equilibrium. Adapted from author’s published work with permission from MDPI [16].

It was found, through comparison to experimental data, that these surface profiles overpredicted roughness. This follows logically from observation of machined surfaces as noted in previous efforts; roughness peaks are generally round, not sharp, as portrayed in Figure 4.3b. To address this discrepancy, profiles were subsequently filtered with a Gaussian filter—the window size of which was adjusted according to the square root of the feed at each condition. The result of this Gaussian filtering on the current profile is shown in Figure 4.4 below.

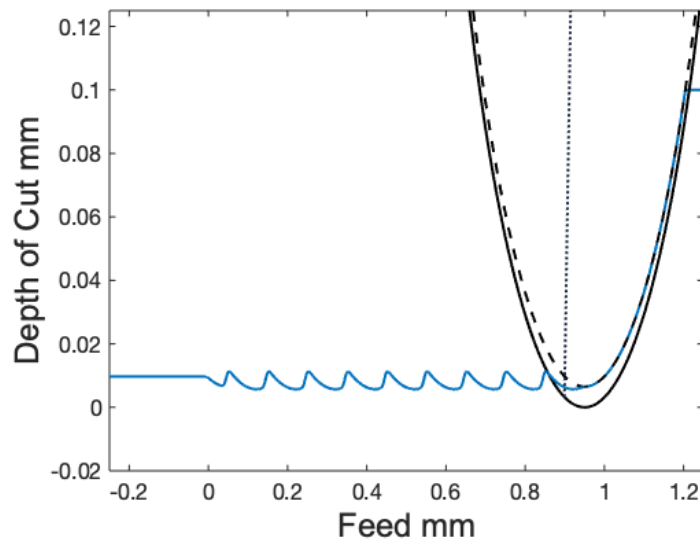


Figure 4.4. Surface profile created by the iterative model, shown at equilibrium after gaussian filtering. Adapted from author’s published work with permission from MDPI [16].

The model then calculates roughness values R_t/R_z and R_a for the profiles under different conditions of nose radius, edge radius and feed. The modeled roughness values are then plotted against the predicted kinematic roughness equation as a function of feed to show the relationship between tool edge radius and kinematically predicted surface roughness on the model predicted values of R_a and R_t/R_z .

4.2.1 Validation of Simulated Surface Roughness

While most of the parameters utilized in this model are easily determined, h_{min} is dependent upon thermomechanical variables and difficult to predict for a given condition. Empirical measurement of h_{min} is most directly achieved by measuring the workpiece spring back on the flank face under plane strain conditions, i.e., orthogonal turning or shaping cuts. Ongoing efforts of in situ characterization are carried out to further improve the accuracy of the h_{min} characterization for different workpiece materials. From such observations, there seems to exist a minimum effective rake angle (y_{eff}) that remains constant as edge radius is varied for a given machining condition. This phenomena has been previously investigated in recent literature [71], and has often been termed as a ratio of h_{min}/r_e , rather than y_{eff} [72, 73]. From these investigations, as well as inverse determination of h_{min} from pedigreed surface roughness data, y_{eff} values and corresponding h_{min}/r_e values, shown in Table 2, were determined. It should be noted that these values are not purely material constants, as they largely vary with cutting interface temperature, which depends on a few variables—of which, material properties and cutting speed are typically deemed most relevant. The cutting speeds used with the materials Al 1075, 51CrV4, and Ti-6Al-4V are 200, 200, and 288 m/min, respectively.

Table 4.1. Material properties, and empirically determined material-specific y_{eff} and h_{min}/r_e values for the workpieces studied.

Material	y_{eff}	h_{min}/r_e (± 0.05)	Ultimate Tensile Strength	Young's Modulus	Thermal Conductivity
AL 1075	-71°	0.06	90 MPa	69 GPa	236 W/mK
51CrV4	-68°	0.07	1950 MPa	190 GPa	46.6 W/mK
Ti-6Al-4V	-67°	0.08	1100 MPa	115 GPa	7.2 W/mK

The measured roughness values from cutting trials described in section 3.1 are shown below in Figure 4.5, compared to the modeled roughness output. The model was

found to be in good agreement with the experimental results for the given range of tool edge radii, with initial deviation from kinematic roughness occurring between 0.8 and 2 μm R_z . Surface finish in all samples was free of major defects when observed optically at up to 50x magnification. As has often been reported by other efforts, larger tool edge radii produced a higher surface roughness at low feeds than small tool edge radii, while generating essentially the same roughness when the measured values approached the conventional, predicted kinematic values. It may be noted that the model slightly underpredicts roughness values across the board, especially as feed increases. This is most likely due to process instability found at higher chip thicknesses.

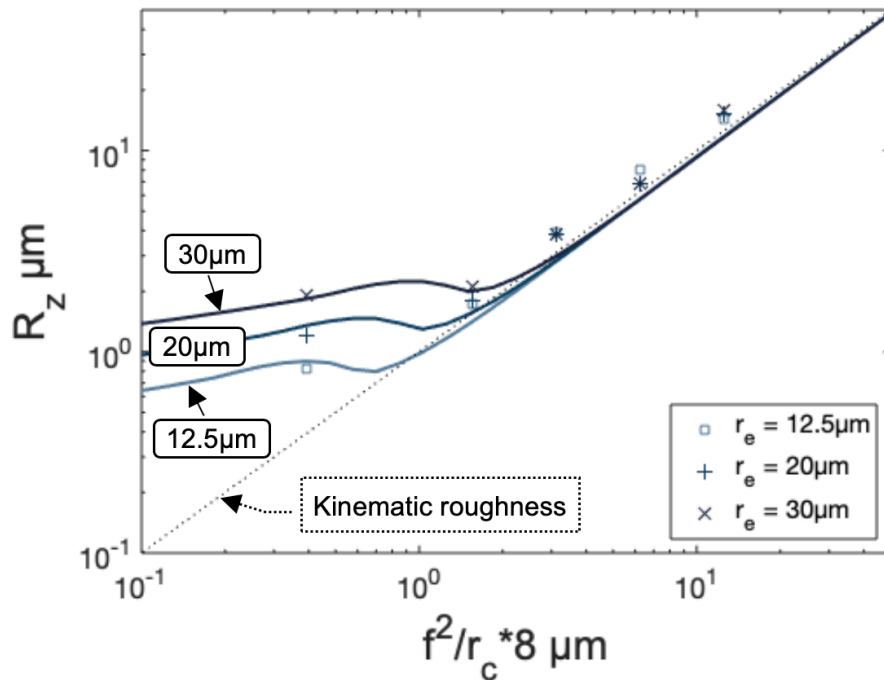


Figure 4.5. Roughness (R_z) model (lines) compared to data gathered through experimental investigation in Ti-6Al-4V. Adapted from author's published work with permission from MDPI [16].

As mentioned above, a key finding of the proposed model is its deviation from the predicted kinematic roughness at a point very near to where actual (measured) roughness values deviate, as shown in Figure 4.5. However, when compared to the data in Figure 4.6, the as-developed model (dashed line) begins to predict values below what is measured, at least when proper ISO surface roughness measurement standards are maintained (i.e., using long evaluation lengths). The causes of this discrepancy are twofold: edge roughness and

machine tool error. The large roughness deviation found by the data from longer evaluation lengths in can be attributed to machine tool error that plays a significant role at low predicted kinematic roughness. While the as-developed, unadjusted surface generation model developed here is still valid for short roughness evaluation lengths (that eliminate the effect of machine tool error/waviness) at these feed rates, the additional (machine/dynamic) error introduces waviness among other artifacts to the standard measurement of R_t/R_z and R_a . This discrepancy is relevant, but not resolved without considering machine dynamics.

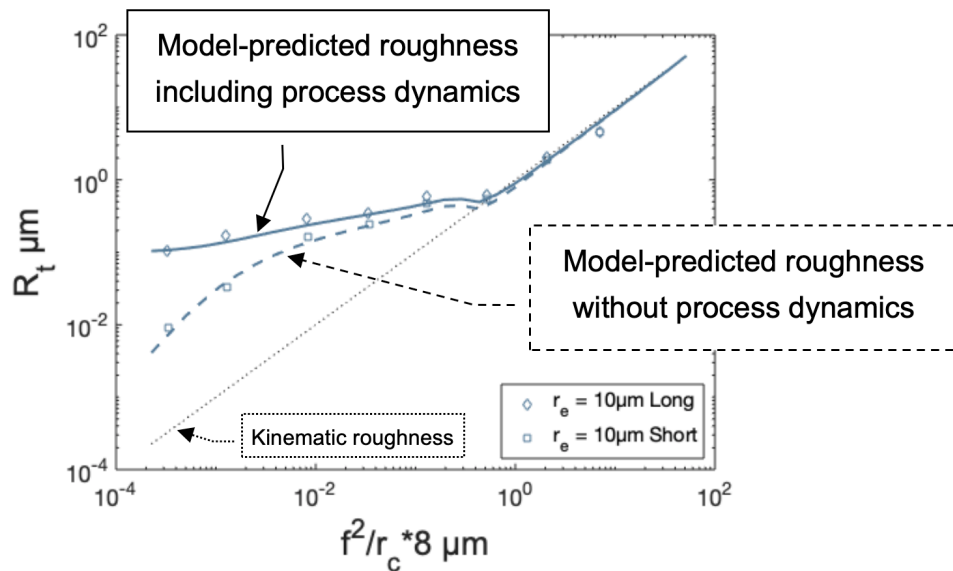


Figure 4.6. Model compared to data adapted from Knuefermann [13], roughness measurements were taken in both long and short formats to show waviness influence on the typical long measurements. Material: 51CrV4. Adapted from author’s published work with permission from MDPI [16].

The use of shorter roughness evaluation lengths is more relevant when evaluating surface generation phenomena (rather than strictly roughness), as the model assumes perfectly spaced, planar toolpaths, unlike those that occur under a dynamically oscillating machine tool/workpiece interface. In comparing the unadjusted model output to the data found by the short evaluation length measurement data in Figure 4.6, it is apparent that some discrepancy still exists at extremely small feed rates (lower than those typically adopted in ‘macroscopic’ finish machining of metals). It is posited this is due to the lack of edge roughness incorporated in the surface profiles generated by the proposed model. This tool edge roughness will cause a relative increase in short evaluation roughness as the

actual roughness reduces past some level. However, as the short evaluation length data in shows, the point at which the roughness begins to deviate is at an extremely low feed, leading to the conclusion that the presented model is likely valid for most new tools of commercial quality. Tool edge roughness does not seem to be a significant factor at the parameter levels found in this work.

Moreover, Knuefermann [13] showed that turning is often capable of creating surfaces that have lower roughness than the tool edge itself. This effect is most likely due to the tool becoming approximately smooth when cutting, as posited in [4]. Upon the entrance of the tool to the cut, small tool defects (typical of new or slightly worn tools) will act as small cutting edges themselves. The material cut by these small edges will be displaced into the defect, promptly filling this region, leading to a much smoother tool edge.

It follows that this unadjusted model is accurate for surfaces generated by tools in even slightly worn condition, when evaluated by short evaluation length roughness methods. It should be noted that while tool edge roughness will play a role in surface roughness generation, it will not be a significant factor until the roughness caused by the tool edge itself is of the same magnitude as the roughness generated by kinematic and side flow effects. Due to machine tool error and side flow effects, it is unlikely that this roughness (under benign tool edge roughness conditions) would contribute significantly to standard roughness measurements of long evaluation length in non-precision applications due to the other effects' heights dwarfing the height of the small surface variations caused by the tool edge roughness.

4.2.2 Incorporation and Validation of Machine Tool Error Dynamic Offset

In comparison to the data gathered by the finish machining of aluminum in [12], the present model's raw output predicts significantly lower surface roughness at low kinematic roughness. As hypothesized by Childs et al., this relative rise in roughness for this dataset is again most likely due to machine tool/vibrational error. Indeed, this data mirrors the roughness trends due to machine tool error (MTE) found over longer evaluation lengths in similar work performed by Knuefermann [13]. Childs et al. [4, 12] utilized rather

long evaluation lengths, similar to the length used in the long assessments in Figure 4.6. Over such an interval, waviness caused by MTE will contribute a substantially to the overall surface roughness measurement. Had these roughness measurements been analyzed with a shorter evaluation length to eliminate waviness components, it is likely the data would be more significantly related to the surface generation-induced roughness, rather than MTE. Visualization of the influence of the typical waviness caused by MTE over low kinematic roughness conditions is seen below in Figure 4.7.

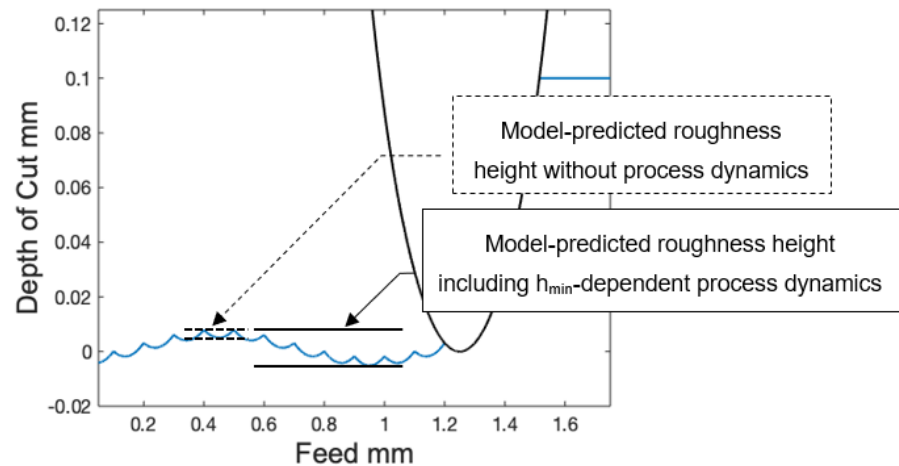


Figure 4.7. Surface profile altered by MTE, typical of way axis-induced error. Adapted from author's published work with permission from MDPI [16].

Inspection of the difference between short and long evaluation length roughness values reveals that MTE (over a given evaluation length) causes a constant offset value of roughness deviation for a given tool/machine combination, as shown in [13]. To correct the model for this discrepancy, MTE was quantified by taking the difference between the model and measured roughness values in very fine finishing conditions (where the relative magnitude of MTE is highest) and added to the model's roughness at every point. This calibration methodology enables the model to approximate MTE-induced roughness deviation for a given machine, tool, and workpiece in light of asynchronous spindle error, way travel error, servo instability, hydraulic vibration, etc. Previous methodologies have performed this calibration by utilizing a vibration sensor placed somewhere near the tool/workpiece interface. This presented method eliminates the need for such measurement by utilizing retroactive surface roughness measurement instead. However, this necessary calibration reduces the efficiency of the roughness model in cases affected by MTE, yet no

accessible technique exists for predicting roughness increases caused by MTE for an unknown machine, tool, and workpiece combination. All such parameter combinations would necessitate independent calibrations.

Upon inspection of different MTE constants for various tool edge radii (while holding all other parameters constant), a logarithmic trend of MTE-induced roughness with respect to r_e was revealed, whereby increasing r_e leads to less MTE-induced roughness in the affected machining regimes. It is thought that the reason for this trend is that of positional error damping caused by increased ploughing forces and vibrational error damping caused by viscoelastic shear-damping behavior, as depicted below in Figure 4.8. A roughness-reducing effect similar to this has also been noted in milling [40].

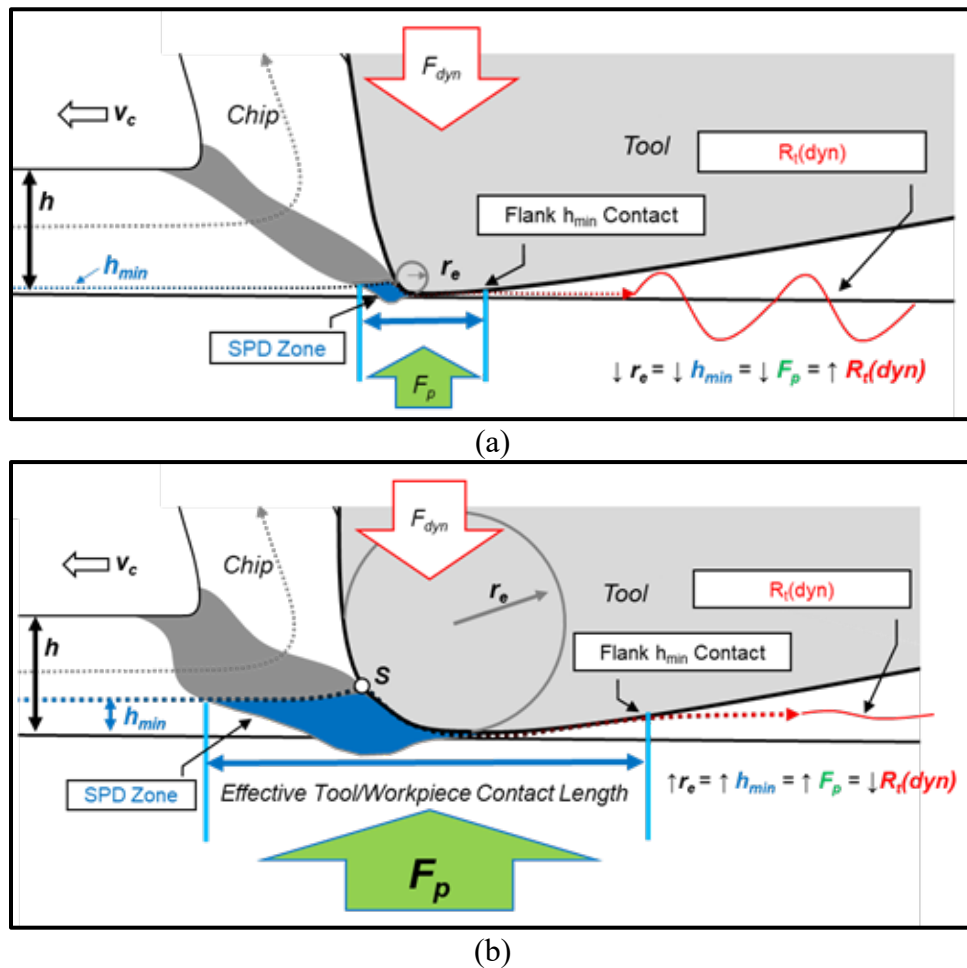


Figure 4.8. (a) Tool/workpiece interface model depicting the tendency of a small edge radius to promote less MTE damping (b) Tool/workpiece interface model depicting the tendency of a large edge radius to result in more MTE damping, proportional to the increase in h_{min} . Adapted from author's published work with permission from MDPI [16].

The mechanism of ploughing forces in the damping of MTE-induced roughness is thought to be due to the reaction of the machine tool to the revolving workpiece and induced via cyclical cutting force variation. Commonly, MTE is found in the spindle or ways. When cutting with these imperfect tools, the engagement of the tool and workpiece in the cut will vary by some amount. When utilizing a small tool edge radius, this engagement variance does not change the ploughing forces appreciably due to the small area where ploughing forces can be developed. The negligible increase in ploughing force causes very little deflection in the machine tool when this small engagement variance is encountered. Therefore, the position of the tool is accurate to the ways and spindle of the machine, and whatever error exists in these elements is “copied” to the workpiece.

Alternatively, when a tool of larger edge radius is utilized on the same machine, an increase in engagement between the tool and workpiece (caused by MTE) will cause more ploughing force, due to the increased amount of material being required to flow under the tool edge. The increased ploughing force will in turn present substantial resistance to dynamic force variations associated with the machine tool and workpiece (F_{dyn}). As the engagement variance is caused by imperfections within the machine tool, deflection response to these engagement variances shall lead to a surface that is a slightly smoother “copy” of the instrument’s axes. Additionally, viscoelastic shear-damping behavior caused by the increased amount of material being plasticly deformed under the tool will substantially dampen sudden positional changes or vibration, such as machine tool harmonic frequencies or asynchronous spindle error. Increased shear damping can also eliminate chatter by inhibiting the progression of vibrational excitation. After this damping trend was incorporated into the model, it was found that it was in good agreement with results from [4], as shown below in Figure 4.9.

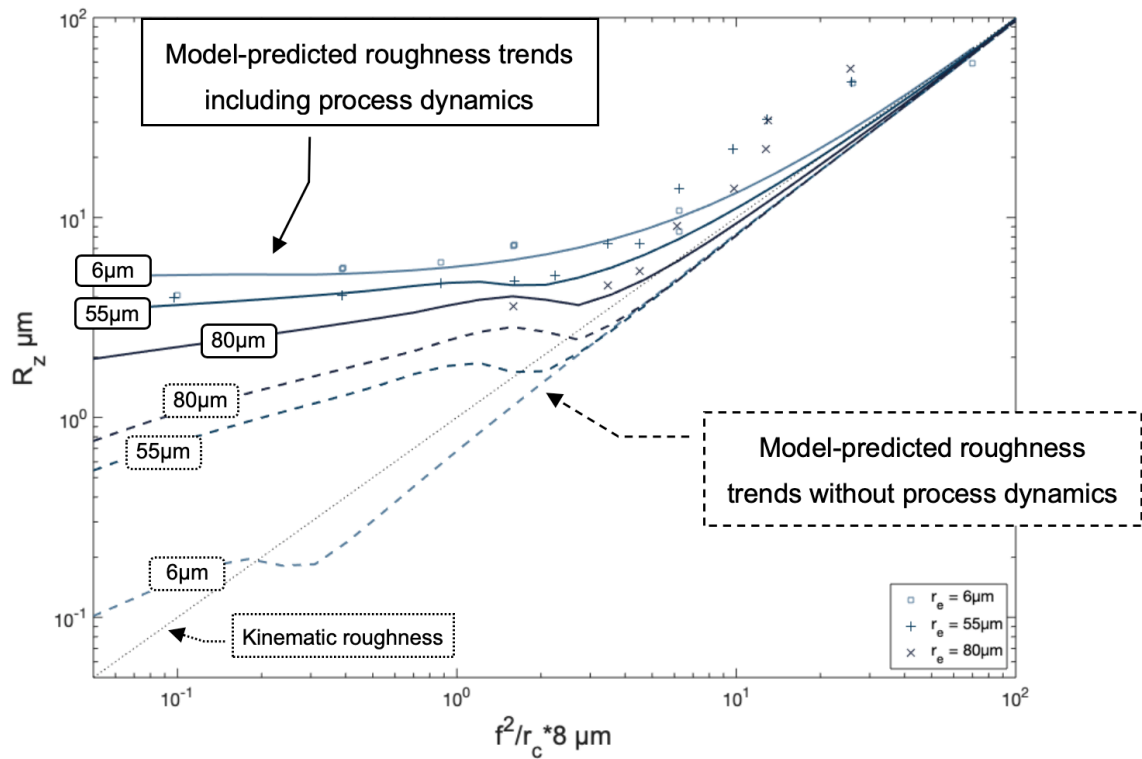


Figure 4.9. Model compared to data adapted from Childs [4], MTE-induced roughness is predicted with some accuracy. Material: Al 1075. Adapted from author's published work with permission from MDPI [16].

These results verify the suggested damping phenomena described previously. The often-noted trend of a large edge radius to increase surface roughness relative to a small tool edge radius is shown to be inaccurate for machining processes heavily affected by MTE. The incorporation of MTE damping effects due to edge radii is shown in Figure 4.9 by the relative difference between the (dashed) unadjusted model values and the (solid) adjusted model values. Smaller edge radii show a significant increase in roughness when adjusted for MTE-induced roughness, while larger radii exhibit a lesser increase when adjusted for MTE-induced roughness. These findings demonstrate that in some cases, surface roughness may actually be improved by utilizing a larger edge radius. While this model appears to capture the data well on the lower end of the feed regime observed here, there is considerable discrepancy at higher feeds. This is also likely caused by MTE as well as some additional instability due to larger uncut chip thickness generally encountered at these conditions. Notwithstanding these small discrepancies, the model approximates the

deviation of surface roughness at low kinematic roughness in 51CrV4 steel, AL 1075, and Ti-6Al-4V.

A major advantage of this model lies in that it may be calibrated to any machine in a trivial manner. This may be achieved by performing a single finish cut with a tool of known cutting edge radius (preferably approximately 10–20 μm , so that the MTE-induced roughness is of a higher relative amplitude) and subsequently measuring the long evaluation length surface roughness of the generated surface. Comparing this measured surface roughness to the value predicted by the unadjusted model will reveal the MTE-induced roughness for this tool edge radius, whereby all other surface roughness values may be predicted for varying finishing parameters, outside of excessive chatter or roughness increasing effects such as inclusions or grain pullout.

4.3 Subsurface Integrity Case Study Correlated to Surface Generation Model Geometry

Further investigation of this geometric model enabled the discovery of geometrically defined multi-pass effects. In Figure 4.10, it may be observed that for a given edge radius, different kinematic roughness values lead to quite different surface conditions. Figure 4.10a shows a surface that has very little overlap between the ploughing areas, indicated by the dashed profiles in the sub-surface; most of the surface is comprised of material that has only been ploughed once, indicating a surface that has been machined efficiently, i.e. with relatively limited ploughing. In Figure 4.10b, the model geometry exhibits a sub-surface that has been heavily ploughed. The entire surface is shown to have been ploughed multiple times as evidenced by the coincident dashed line profiles. While the surface appears to be smoother due to the larger nose radius, this surface has been ploughed to a much greater extent, which is known to generate additional heat and strain hardening, which may lead to altered sub-surface characteristics.

What follows is an investigation into the relationship between the model geometry and the observed subsurface material alteration in Ti-6Al-4V. While this investigation only gives insight into the nature of subsurface alteration in this particular metal, the relationships between the subsurface characteristics to the various model geometries implicate that similar effects may occur in the machining of other metals.

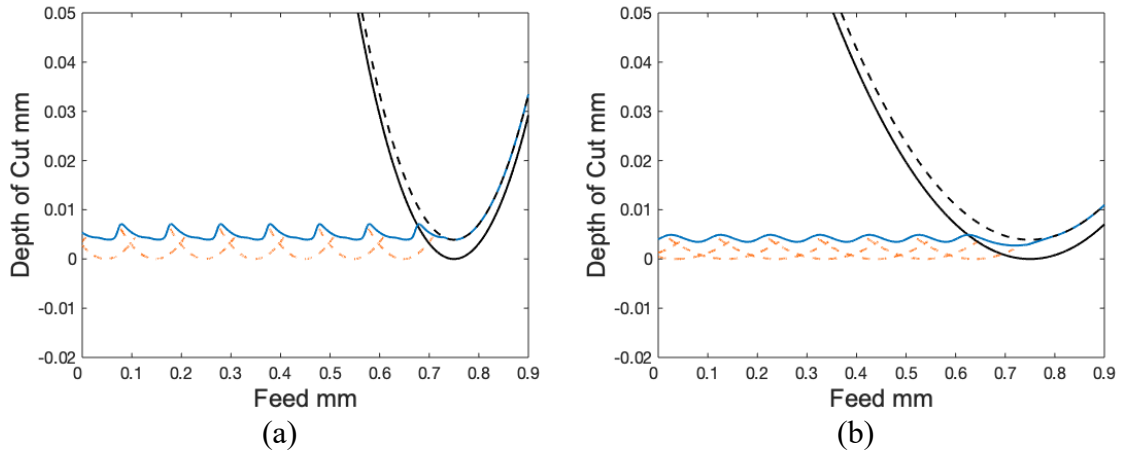


Figure 4.10. (a) Surface model showing the tool profile depth and light overlapping of previous passes, modeled with $r_c = 0.4$ mm, $h_{min} = 5$ μm , and $f = 0.1$ mm; (b) Surface model showing heavy multi-pass condition, modeled with $r_c = 1.6$ mm, $h_{min} = 5$ μm , and $f = 0.1$ mm. Adapted from author's published work with permission from MDPI [16].

4.3.1 Subsurface Microhardness

In order to view the relationship between the model geometry and the subsurface quality, the microhardness depth profile of each sample was investigated. While not an all-encompassing metric, hardness is used here as a prominent quality which displays the nature of the surface alteration, and gives insight into how manufacturers might adjust machining parameters in order to generate subsurfaces of differing quality. The material microstructure of each sample was relatively unchanged; therefore, the perceived hardness alteration is considered to be caused by strain hardening and residual stress alone. Representative sample images showing the lack of major microstructure alteration in both gentle and relatively abusive conditions are shown in Figure 4.11.

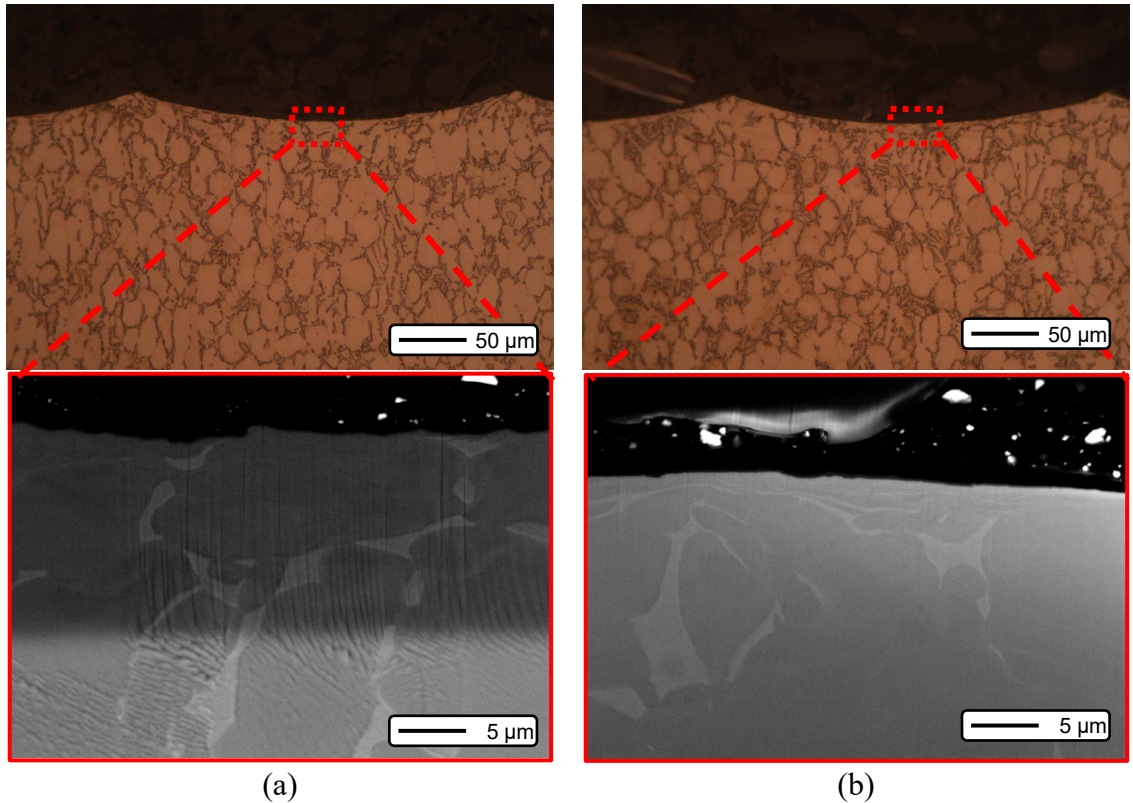
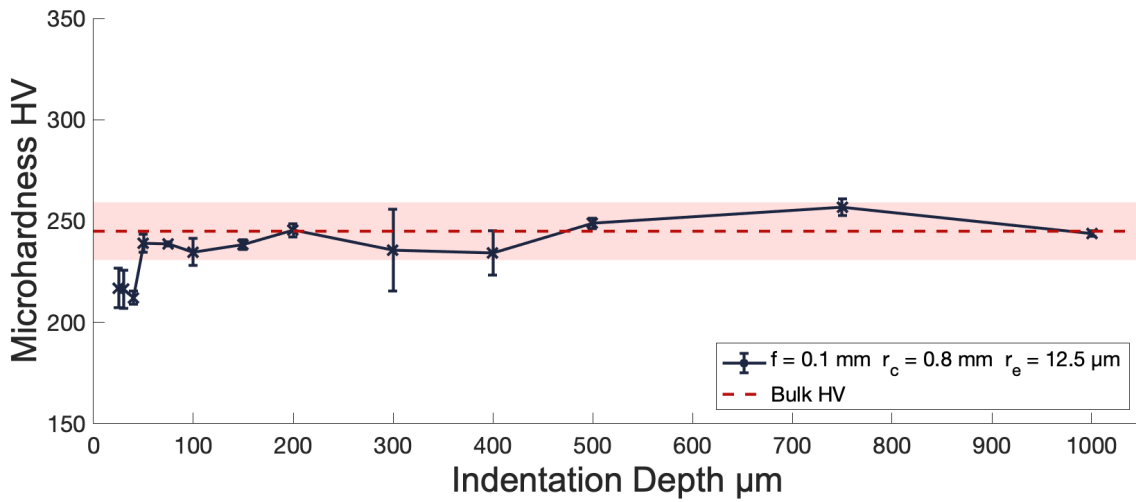


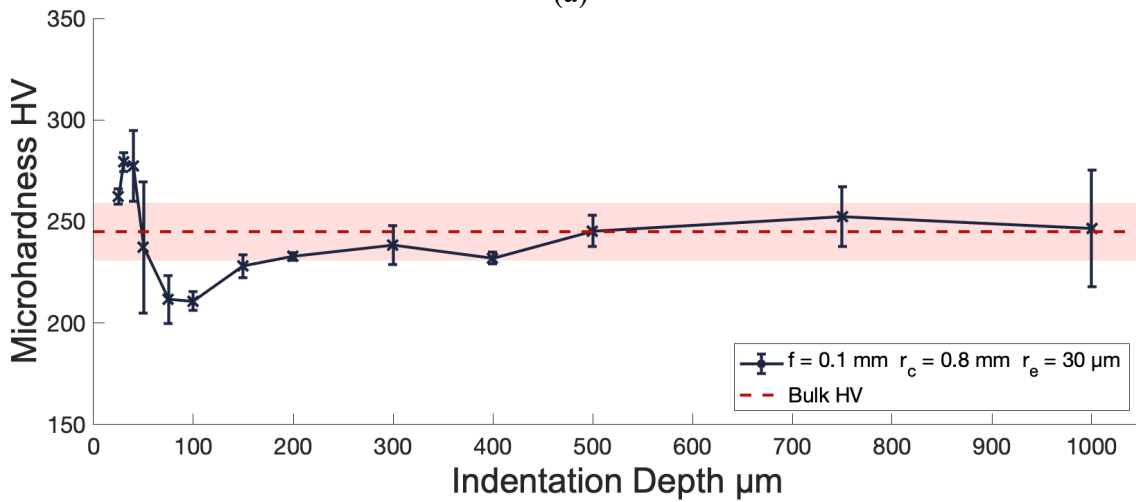
Figure 4.11 Etched and FIB-skimmed samples showing the relative lack of microstructural damage occurring at (a) gentle conditions and; (b) relatively abusive conditions.

Figure 4.12a shows a microhardness profile generated by machining parameters representative of conventional finish machining operations. The profile displays a slight softening very near the surface, but quickly transitions to the bulk hardness value (~ 247 HV). This is similar to results previously obtained in literature [61, 74]. The decrease in hardness near the surface is generally well-accepted as being caused by thermal activity due to the deformation of metal near the tool-workpiece interface. Turning to Figure 4.12b, we see that this softening effect is now obscured due to some phenomena caused by an increase in the cutting edge radius, r_e . While a section of the subsurface depth is certainly seen to be thermally softened, this softened region is extended deeper into the workpiece, and approaches the bulk microhardness value around $300 \mu\text{m}$. This is an implication that the material removal process has been performed such a manner which exacerbates the thermal softening mechanism of the material removal process. However, despite this increased thermal load, there exists a small region nearest to the surface which was found to be harder than the bulk. This implies that significant strain hardening has occurred within

the workpiece material, relative to the sharper condition in Figure 4.12a. This phenomenon is well documented in previous literature [61, 75-77]. Investigations on the influence of cutting edge radius on subsurface hardness by orthogonal machining reports that edge radius is highly significant in determining the magnitude and behavior of this phenomenon. However, this study found that other factors are relevant in workpiece hardness alteration, and in some cases, dwarfed the significance of cutting edge radius' influence on subsurface hardness.



(a)



(b)

Figure 4.12. (a) Microhardness profile of surface with slight thermal softening;(b) microhardness profile of surface with moderate strain hardening.

Microhardness profiles for surfaces generated by carbide tools of the same geometry as those used in Figure 4.12, but with coarser feed, are shown in Figure 4.13. An overall trend of softening near the surface may be noticed, with neither of the profiles

displaying a hardened region near the surface. Indeed, it is apparent that both machined surfaces experienced thermal softening near the machined surface, but the hardness profile of the surface generated with the sharper tool shows softening of greater magnitude as depth increases. However, the hardness profile of the workpiece machined with the larger cutting edge radius (Figure 4.13b) remains relatively harder near the surface than the profile found in the workpiece machined by a sharper tool (Figure 4.13a). Therefore, the trend of the larger cutting edge radius to create relatively harder near-surface material still exists, but the increase in feed value diminishes the relevance of this factor.

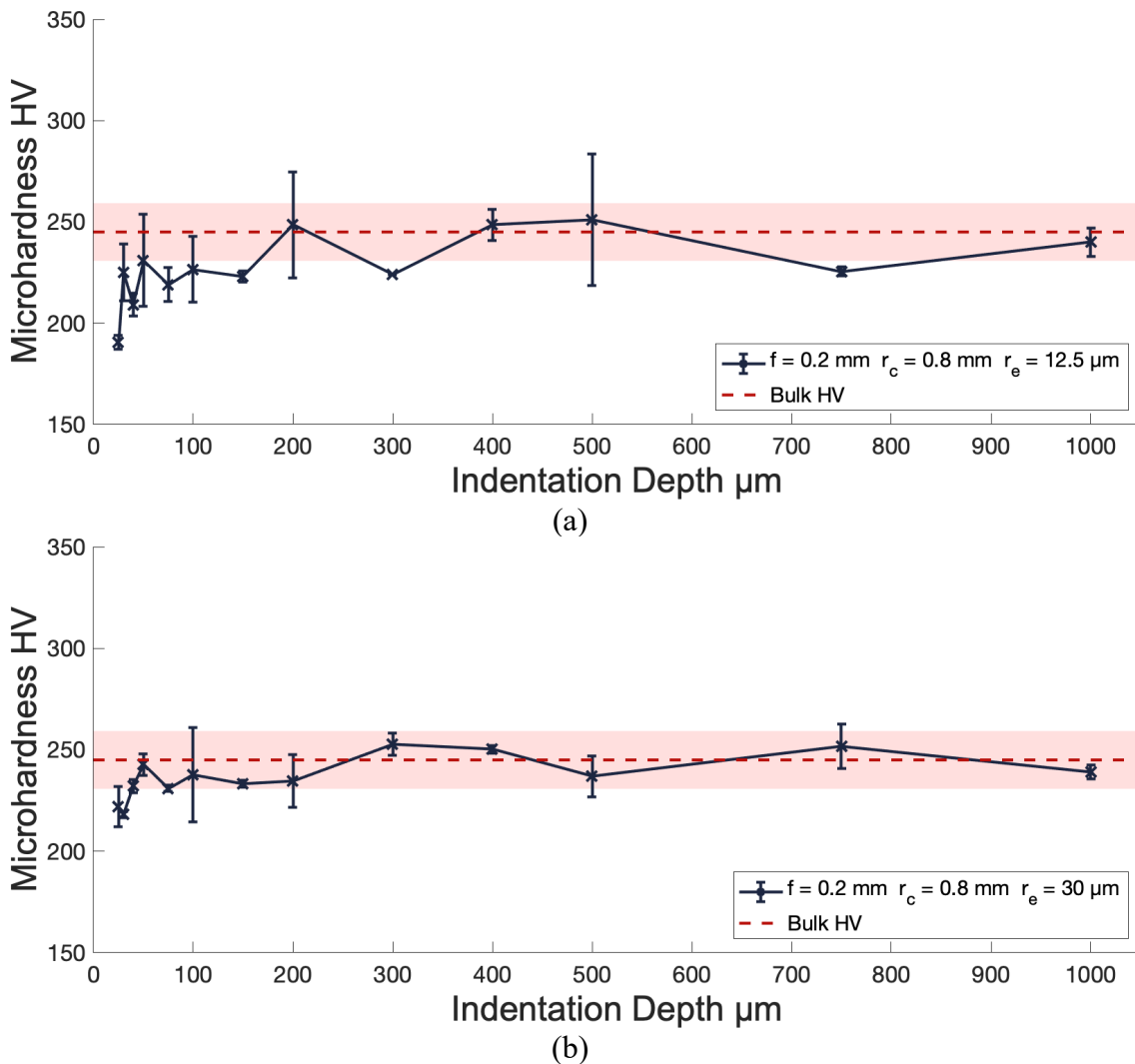
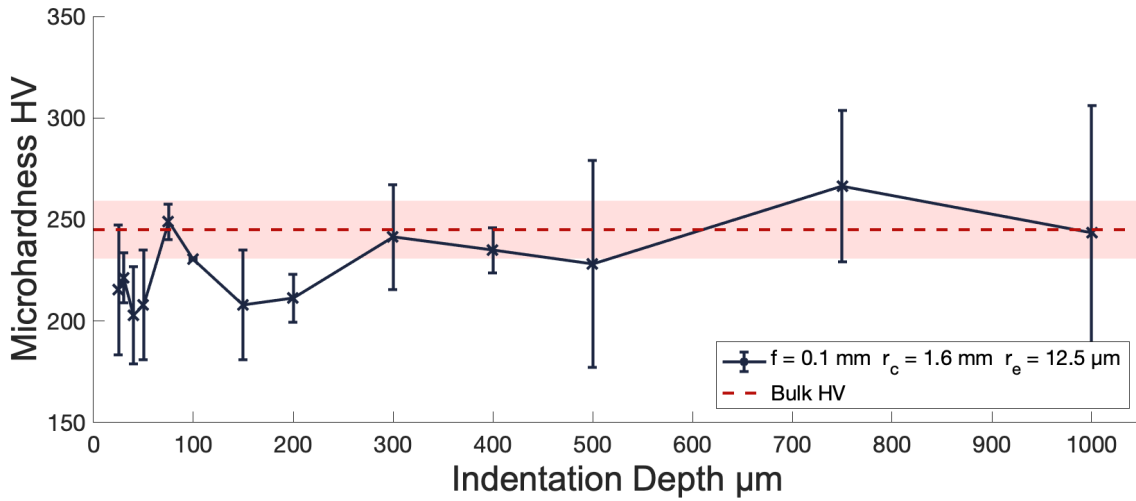
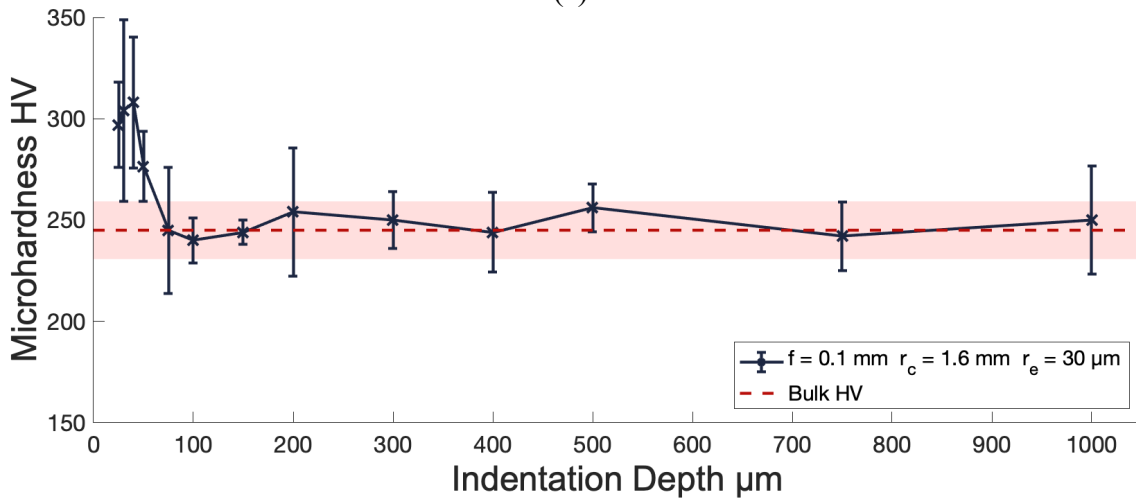


Figure 4.13. (a) Microhardness profile of surface with thermal softening;(b) microhardness profile of surface with slight thermal softening.

On the other hand, a trend of increasing hardness corresponding to increasing nose radius was found when the tool nose radius was increased, and feed remained the same. Contrasting Figure 4.14b with Figure 4.12b reveals that the same cutting edge radius value creates surfaces of significantly higher surface hardness. This workpiece also displays a lack of thermal softening through the depth as has been seen in all other samples shown here. It is hypothesized that this is due to the higher levels of strain incurred in the material near the machined surface. Alternatively, the surface machined by a sharper tool of the same nose radius led to a hardness profile (Figure 4.14a) that appears similar to the profiles previously generated by the 12.5 μm cutting edge radius tools. However, the thermally softened material is of lower hardness, and extends into the depth of the workpiece far deeper than the profiles observed previously.



(a)



(b)

Figure 4.14. (a) Microhardness profile of surface with substantial thermal softening;(b) microhardness profile of surface with significant apparent strain hardening.

Thus, there exist various relationships between the subsurface material hardness and the finish machining parameters varied in this study. Generally, increases in cutting edge radius, corner/nose radius, and decreases in feed lead to apparent hardness increases at the surface. These trends also generally cause an increase in side flow, and overall ploughed material within the current surface generation model. It was hypothesized that the length of the side flow modeled within the geometric model would correlate well to increases in hardness. Similar to the observed hardness behavior, this length increases with cutting edge radius and corner/nose radius and decreases with feed. However, this side flow length corresponds to the ploughing conditions of just one machine tool path segment. Considering that each adjacent machine tool path segment would incur an additional

amount of strain hardening, and that each feed value would have differing path segments for a given area, this side flow length was multiplied by the number of paths per millimeter (or divided by feed). The values generated by this method were then normalized, as this value is simply a geometrical relative quantity, with no direct numerical relationship to actual strain or other material properties. Consequently, this quantity is termed a ‘ploughing constant’. In Figure 4.16b and Figure 4.17b, this predicted ‘ploughing constant’ is plotted against tool edge radius for the various conditions discussed, so that its behavior may be compared to that of the subsurface hardness increase for these same conditions. An example of the determination of this value is shown in Figure 4.15.

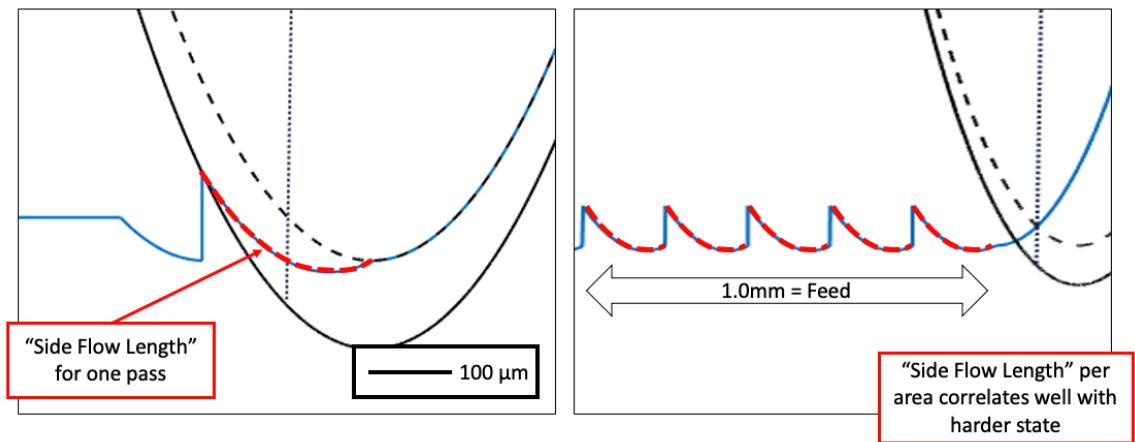


Figure 4.15. Determination of the ploughing constant for a given surface.

Based on the results shown in Figure 4.16, the trends displayed by the ‘ploughing constant’ model agree with the observed microhardness behavior for feed = 0.2 mm. While the representation is not exact and does not indicate any numeric hardness value, the increase of hardness for decrease in corner radius and slight increase in hardness for increases in tool edge radius are well captured by the model.

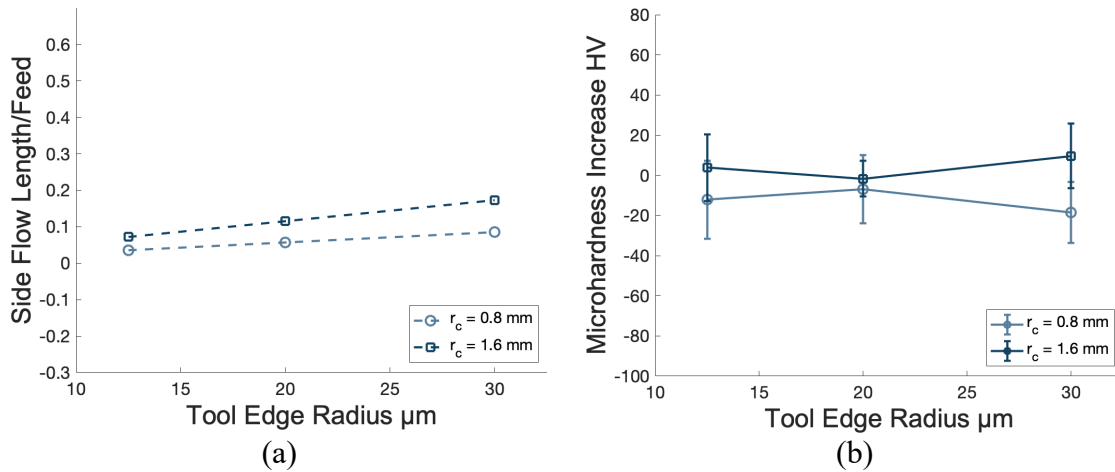


Figure 4.16. Hardness trends plotted against tool edge radius for $f = 0.2$ mm (a) model predicted ‘ploughing constant’ and (b) observed microhardness data. Relative hardness alteration is of small magnitude due to large f .

Comparing the ‘ploughing constant’ model to data captured at feed = 0.2 (Figure 4.17a and b), the trends of the model relative to the machining parameters capture the hardness behavior very well. The increase in hardness due to tool cutting edge radius is apparent in both the model and data, as is the hardness increase due to the increase in corner radius. It should be noted that the axes in all graphs listed in Figure 4.16 and Figure 4.17 are static, and the relative magnitudes (locations) of each point are preserved. Comparing each of these figure sets, it is obvious that the model predicts that the hardness increase will be much more variable when finer feed conditions are used. The data gathered from each sample’s surface hardness increase showed this predicted trend with very good agreement.

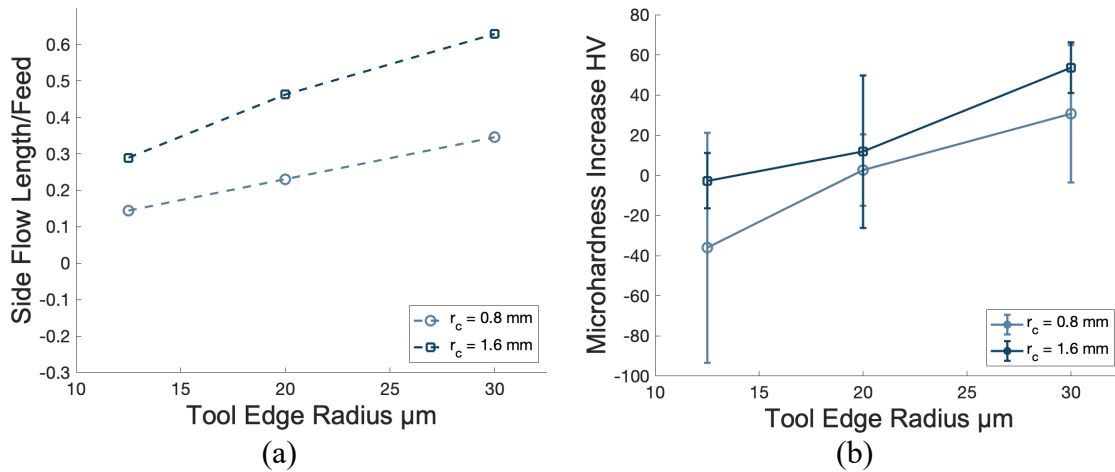


Figure 4.17. Hardness trends plotted against tool edge radius for $f = 0.1$ mm (a) model predicted 'ploughing constant' and (b) observed microhardness data. Relative hardness alteration is of large magnitude due to small f .

Therefore, all selected parameters significantly affect near surface hardness. Higher machining-induced hardness in Ti-6Al-4V may be achieved by increasing the cutting edge radius, increasing corner/nose radius, and decreasing feed. In the data gathered in this investigation, higher feeds lead to less distinction between edge conditions, indicating an interaction between edge radius and feed. Nose radius did not affect the increase in hardness between different cutting edge radius conditions, yet generally caused a static offset increase when enlarged.

Thus, the geometric parameters elaborated on here are all of importance to surface integrity and should be considered when selecting machining parameters in finish machining when subsurface integrity is considered relevant. Moreover, the geometry of the currently developed model (already verified in the prediction of surface roughness) correlates well with the observed strain hardening trends. While this 'ploughing constant' model analysis does not necessarily lead to specific values of hardness, it does allow for improved relative understanding of hardness behavior in Ti-6Al-4V, and may be used as a framework for future works seeking to establish more exact predictions of material properties.

4.3.2 Subsurface Hardness Variations in Feed Direction

In order to further investigate the presence of three-dimensional effects in finish machining, nanoindentation fields (and their subsequent contour maps) were used to analyze the near surface hardness of the machined subsurfaces. Previous studies in machining-induced microhardness have solely investigated the variation in microhardness as it relates to depth (distance away from the machined surface). The previous section 4.3.1 is an example of the scope of such analysis. Figure 4.18 shows both model predicted surface profile topography, and a contour map of the hardness values of the material over the presented two-dimensional subsurface, attained by nanoindentation. Please see section 3.2.1 and Figure 4.10 for orientation to the machined subsurface geometry presented here. The contour map topography reveals that near surface hardness does in fact vary substantially in the feed direction. Most of the conditions investigated by this method in Ti-6Al-4V showed a similar pattern as can be seen here. That is, there exists some concentrated area of hardened material directly under the feed mark troughs. Figure 4.18a shows that in the conditions with machining parameters which induced less overall ploughing (low nose radius, high feed and low cutting edge radius), periodic variation of hardness congruent with the feed value persists in the material subsurface all through the area measured here. However, the absolute magnitude of the variation can be seen to drop quickly with increasing workpiece depth. On the other hand, Figure 4.18b shows a surface that maintains harder material values through the depth of the sampled area, while still showing the periodic variation of hardness with feed as noted previously. These overall hardness results agree well with previously established trends discussed in section 4.3.1.

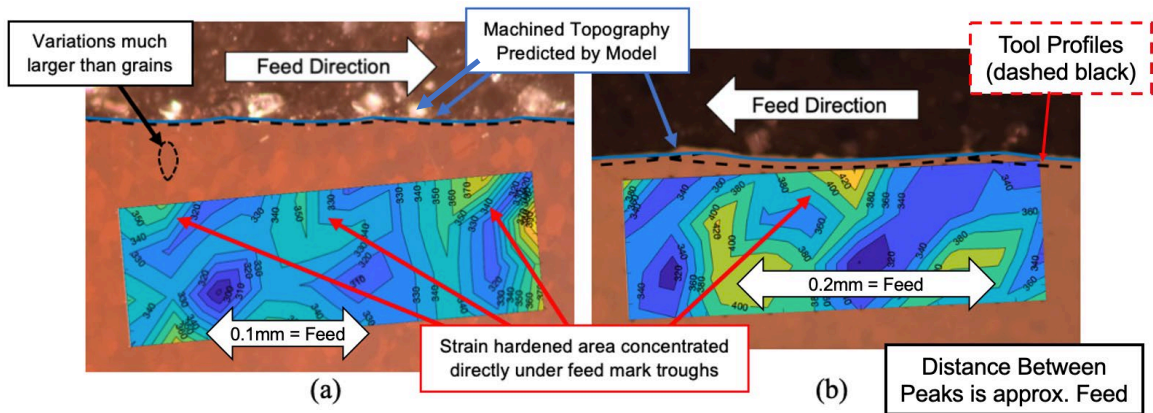


Figure 4.18. Three-dimensional subsurface hardness profile for machining conditions: (a) $r_c = 0.4$ mm, $f = 0.1$ mm, $r_e = 12.5$ μm ; (b) $r_c = 0.8$ mm, $f = 0.2$ mm, $r_e = 30$ μm .

However, in samples where the overall subsurface hardness showed a marked increase relative to the overall data set observed here, it was found that the subsurface hardness variation behavior changes substantially. Figure 4.19 shows one such sample. Similar to the trends observed in Figure 4.18b, the hardness behavior in Figure 4.19a shows that machining-induced material hardness increase extends far into the depth of the evaluated material. However, the periodic nature of the hardness is found to have been altered due to additional ploughing phenomena. Rather than vary at a period equal to the feed value, it seems that in cases of surfaces with higher calculated ‘ploughing constants’, the period of near surface hardness variation was double the feed value. It is hypothesized that this additional hardness spike at the peak of the feed marks is caused by excessive ‘double ploughing’ of the material in these regions, as shown in Figure 4.19b. It is theorized that this mechanism is partially responsible for the observed increase of one dimensional hardness profiles at higher corner radius and lower feed, as found previously in section 4.3.1.

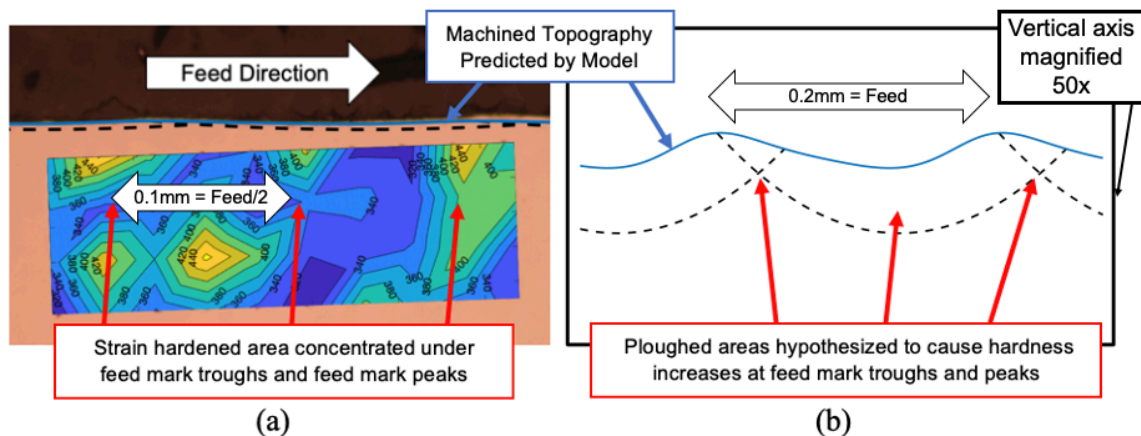


Figure 4.19. (a) Three-dimensional subsurface hardness profile for machining conditions: $r_c = 1.6$ mm, $f = 0.2$ mm, $r_e = 20$ μm ; (b) magnified model subsurface geometry for this condition.

While it is thought that the periodic hardness variation noted here has implications for surface integrity, no published work has yet provided any data correlating this variation to fatigue life, wear, or corrosion resistance. At minimum, this data gives insight into how the hardness increase near the surface is distributed, and therefore a better understanding of the causes of measurement inaccuracies of microhardness testing is attained. In order to improve the statistical significance of results in future microhardness efforts which follow the conventional method of solely investigating the behavior as a function of depth, it is recommended that microhardness be evaluated at the same position on each trough. However, considering the discovery of periodic hardness variation in the subsurface of all samples, it should be acknowledged that one dimensional hardness inspections do not give the full picture of subsurface phenomena induced in finish machining of Ti-6Al-4V, and most likely all other ductile-machining metals. Though typical one dimensional ‘depth’ analysis of hardness behavior is useful for determining overall trends, it appears that hardness behavior in the feed direction is also relevant in the analysis of more geometrically complex operations such as turning or milling. Full surface integrity analysis should include geographical observations of the subsurface material variations when possible, in order to deconvolute their relationships to process parameters, as well as the performance of the machined part.

CHAPTER 5. CONCLUSIONS AND OUTLOOK

While this work is not the first to identify the relevant size effects in surface generation during finish machining, the role that each effect plays with respect to surface integrity has been clarified. In particular, the effects of side flow and material spring back have been shown to be of high importance to finish machining induced surface integrity. Hence, the influences of three-dimensional parameters are significant, both in the observed surface roughness in finish machining in general, and in the machining-induced subsurface characteristics in Ti-6Al-4V.

Varied cutting edge geometry was discovered to affect the final machined topography in multiple ways. In many cases, increased cutting edge radius was found to increase surface roughness due to the occurrence of side flow at the free edges of the cut. However, while cutting edge radius generally increases roughness in high-precision machines, in machines affected by machine tool error, edge radius was shown to decrease observed roughness. This effect was investigated and is considered to be caused by process damping that results from viscoelastic shear-damping, as well as elastic damping that propagates through the machine/workpiece dynamic system.

By adjusting machining parameters, it was found that near surface hardness can be changed with some degree of confidence in the finish machining of Ti-6Al-4V. Generally, increases in corner radius, increases in cutting edge radius, and decreases in feed were all found to increase the hardness value of the material near the machined surface. The effects of feed and cutting edge radius were prone to interaction, whereby a decrease in feed caused the hardening/softening effect of increased/decreased cutting edge radius to be of greater magnitude for a given edge radius change. While these effects are still apparent to some extent in rougher machining regimes, it was found to be of much greater relevance in fine finishing conditions.

Additionally, two-dimensional subsurface hardness behavior was observed and analyzed. In addition to the usually investigated depth-direction hardness variation, variations of hardness in the feed direction were discovered, and found to vary significantly with multiple machining parameters. Strain hardened regions were typically observed

directly below the feed mark troughs in most conditions. While the variation was seen to directly correlate with feed for conditions which induced relatively little ploughing, other conditions led to a halving of the variation period. These additional hardened regions occurred under the peaks of the feed marks and are hypothesized to be caused by “double-ploughing” of material occurring in these areas.

This work also presents an iterative geometric surface generation model for the prediction of surface integrity in finish machining, built upon unique assumptions about the size effect in machining. The presented model considers the engagement and geometry of the tool and workpiece in light of complex ploughing mechanisms that give rise to side flow and material spring back. In this sense, it is fitting to consider this model qualitatively ‘physics based’, as it incorporates the dominating physical phenomena which lead to the generation of the machined surface. The model establishes a novel method for modeling relatively complex, MTE-influenced surface roughness values that are dampened by tool edge radius. Complex surface integrity effects, such as strain hardening, thermal softening, recrystallization, and residual stress evolution are intimately tied to the surface generation mechanics, which the present model appears to accurately capture.

Within the cutting parameter range under investigation, comparisons with experimental data showed that the presented model predicts surface roughness with good agreement. Given precise roughness data, estimation of minimum uncut chip thickness is possible via reverse fitting of the model. While not a direct method, the results achieved by this methodology correlate well with the observed minimum uncut chip thickness, and give insight into the relative differences of minimum uncut chip thickness between different materials. Additionally, the geometry of this model was also found to correlate very well with subsurface phenomena. In particular, the calculated ‘ploughing constant’ matched the relative overall hardness increase behavior with good agreement. Furthermore, the presence of strain hardened regions directly below the feed mark troughs, as well as peaks (when substantial double ploughing was present there) verified the relevance of the model’s geometrical assumptions.

Altogether, three-dimensional finish machining processes like turning and milling are shown to have the potential to be more than substitutes for costly machining processes

such as grinding. Rather, given a better understanding of surface generation size effects, conventional finish machining may also be employed as a means to create longer-lasting parts and eliminate costly post-processing steps, both of which lead to increased sustainability. Two size effects, material side flow and spring back, significantly influence the surface integrity of finish-machined surfaces and are directly affected by geometric machining parameters. In many cases, improved surface integrity at fine feeds may be reliably achieved by altering machining parameters in a trivial manner. The model resulting from this study allows for increased understanding of the mechanisms leading to surface integrity in three-dimensional finish machining processes, and should provide a basis for selecting parameters that produce surfaces of smooth, resilient topography.

5.1 Future Work

While the quantitative prediction of subsurface material properties like hardness and residual stress lies outside the scope of the present study, the geometric ‘boundary conditions’ of the tool/workpiece engagement are predicted quite well with the proposed geometric model. Therefore, subsequent work will focus on expanding the current model to provide inputs to the author’s research group’s concurrently developed thermo-mechanical surface integrity models, which require knowledge of multi-path effects and full-surface ploughing insight identified in this work.

Additionally, further investigation of the newly discovered “two-dimensional” hardness variation is warranted. It is hypothesized that this behavior will be present for all materials machined in a plastic manner, and that this material property will in fact influence component performance substantially. Therefore, subsequent work will focus on identifying this behavior in multiple materials, as well as identifying any relationships this behavior has with fatigue failure, wear, or corrosion resistance.

¹Sections 2.2.1, 3.1, 3.3, 4.1, and 4.2 are partially adapted from author’s previously published work with permission from MDPI [16]

APPENDIX

```
%Surface generation model

% Version 10 mods
% Cleaned up

clc
clear variables

figure(2)
clf
figure(1)
clf
figure(3)
clf
figure(4)
clf

colorpalette = [86,125,156;15,65,98;28,38,65;144,163,180;184 15
10]/255;

%INPUTS@@@@@@@@@@@@@@@@@@@@@@@@@@@@@@@@@@@@@@@@@@@@@@@@@@@@@@@@@@@@@@@@@@@@@@@@@@@@@@@@@@@@
@@@@

% This program is adaptable to a variety of inputs. Measurements begin
% breaking down when too high a hone is created, giving way to
burnishing.

% Input hones and nose radius values here
hone_list = [5;10;20;80];% [µm]
noserad_list = [0.4]; % [mm]

% desired upper feed bound? [mm]
upfeed = .2;
% desired lower feed bound? [mm]
lowfeed = .01;
% desired resolution of feed vs roughness model?
res = 10;
% How many passes should you allow at max? (Program exits after
equilibrium
% is established, however this will serve as a hard stop if that does
not
% occur.)
MaxPasses = 10000;
% DOC for the cut
doc = .25;
% resolution of model profiles
profileres = 300000;
% Critical effective angle, different for different materials and
speeds
criteff = -70; %degrees
% Give one or two values to average for the estimation of
DMTErz(1) = 0;
DMTErz(2) = 0;
```

```

% what edge radius were these measurements taken from?
DMTErz_re = hone_list(1);
%what percent of the sideflow chip will become true sideflow? That
is...
%will exit to the side of the tool(i,j), on top of the surface.
sideflowsusceptability = 1.00; % 1 is 100 percent

%
CALCULATIONS@@@@@@@@@@@@@@@@@@@@@@@@@@@@@@@@@@@@@@@@@@@@@@@@@@@@@@@@@@@@@@@@@@@@@@@@
@@@
% Preallocating
honelevels = length(hone_list);
noselevels = length(noserad_list);
hmin(1:honelevels) = NaN;
DMTEdamped(1:honelevels) = NaN;

% Calculation of average dynamic machine tool error
DMTEdamped(1) = mean(DMTErz);

% Assuming that this data will always be the smallest edge (because it
should
% be in order to get the most accurate measurement) we calculate the
% relative damping of the other edges

for er = 1:honelevels
hmin(er) = (hone_list(er)-hone_list(er)*cosd(90+crityeff))/1000;
if er > 1
relativehonediff = hmin(1)/hmin(er);
DMTEdamped(er) = log(relativehonediff-.06)/log(2.6) + 5.2;
end
end

% Keep this updated for documentation purposes
DMTEdampedchar = "log(relativehonediff-.06)/log(2.6) + 5.2";
% Creating logspace of desired feed range in mm.
doe(:,2) = logspace(log10(lowfeed),log10(upfeed),res);

%initial setup of data file, put at beginning of program
%to simplify
Model8_fullfactorial{1,1} = 'ModelData';
Model8_fullfactorial_Profiles{1,1} = 'ProfileData';
for p = 1:noselevels
Model8_fullfactorial{p+1,1} = strcat('rc = ',
num2str(noserad_list(p)));
Model8_fullfactorial_Profiles{p+1,1} = strcat('rc = ',
num2str(noserad_list(p)));
end
for p = 1:honelevels
Model8_fullfactorial{1,p+1} = strcat('re = ', num2str(hone_list(p)));
Model8_fullfactorial_Profiles{1,p+1} = strcat('re = ',
num2str(hone_list(p)));
end

```

```

% Computation
for hone_r = 1:honelevels
for nose_r = 1:noselevels

%doe construction for a given tool geometry
for b = 1:res
doe(b,1) = noserad_list(nose_r);
doe(b,3) = hone_list(hone_r);
end

%Preallocating for feeds loop: t = 1:res

figure(5)
clf
figure(6455147)
clf

theta(1:res)=0;
ltheta(1:res)=0;
sideflowtot(:,:)=0;
figur = 0;
psharp(:) = 0;

RaModel(1:res,1) = NaN;
RzModel(1:res,1) = NaN;
RaTh(1:res,1) = NaN;
RzTh(1:res,1) = NaN;
RaTh(1:res,1) = NaN;
RaBrammertz(1:res,1) = NaN;
psharp(1:res,1) = NaN;
surfacemean(1:res,1) = NaN;
Profilematrix(1:profileres,1:3*res) = NaN;
del_xp(1:res,1) = NaN;

for t=1:res

figur = figur +1;
%Hone in um
hone = doe(t,3)/1000;
%Tool nose radius in mm
R = doe(t,1);
%Feed in mm
F = doe(t,2);

% % % % % % % % % % % % % % % % % % % % % % % % % % smoothing
length adjust in [mm]
smoothlength =F^(1/2)/12*(R/.4) + hone/100;
% Keep this updated for documentation purposes
smoothlengthchar = "F^(1/2)/12*(R/.4) + hone/100";

% Preallocating for the passes loop
tool(:,:) = 0;
surf(:,:) = 0;

```

```

surface(:, :) = 0;
angle(:, :) = 0;
xp(:) = 0;
xpangle(:, :) = 0;
ypangle(:, :) = 0;
THsideflowarealengthx(:, :) = 0;
sideflowextgapvol(:, :) = 0;
startiroughpre = 0;
stopirough = 0;
startirough = 0;
cv = 0;
skip = 0;
SFRPTRACKx(:)=0;
SFRPTRACKy(:)=0;
SFRPTRACKi(:)=0;

%Minimum Chip thickness in mm:

h =(hone-hone*cosd(90+crityeff));

%angle to show where the sideflow chip begins
ltheta(t) = asin(F/(R-h)/2);
%angle used to line the sideflow chip segment up to the y axis, to make
%calculations easier, this theta transposes the system to some
orientation.

for j = 1:MaxPasses
if skip == 0
pk = 0;
pk2 = 1;
sideflowstopx=0;
sideflowstopy=0;
sideflowstartx=0;
sideflowstarty=0;
sideflowintcount = 0;
sideflowint = 0;
sideflowextintcount = 0;
sideflowextint = 0;
sideflowextgapheight = 0;
sideflowextlength = 0;
sideflowextgapvoltemp =0;

% OLD SURFACE, tool and sideflow vol
for i=1:profileres

if j == 1 %one of these vectors is created for each radius and feed
setup.
xp(i)= (i-1)/profileres*(R*3+50*F)-(R);
xpsub(i)= (i-1)/profileres*(R*3+50*F)+smoothlength/2;
if i == 3
del_xp(t) = xp(3)-xp(2);

% Figures out how many i's are necessary to get to the specified length,
% smoothlength

```

```

gausscurvelengthi = ceil(smoothlength/del_xp(t)/2);
gstd = gausscurvelengthi/3;

% creating gaussian curve with normpdf
ig = (-gausscurvelengthi:1:gausscurvelengthi);
yg = normpdf(ig,0,gstd);

figure(6455147)
hold on
plot(yg)
end
end

%Loop to create starting workpiece model
if xp(i) > 0 && j == 1 && cv == 0 && ((R-h)^2-(xp(i)-F/2)^2) >= 0
surface(i,j) = -sqrt((R-h)^2-(xp(i)-F/2)^2) + (R - 0);

if surface(i,j) >= doc
surface(i,j) = doc;
cv = 1;
end

elseif xp(i) <= 0 && j == 1 && ((R-h)^2 - (F/2)^2) >=0
surface(i,j) = R-((R-h)^2 - (F/2)^2)^.5;
elseif cv == 1 && j == 1
surface(i,j) = surface(i-1,j);
end

% creating tool(i,j) geometry for this pass
if xp(i)>(F*(j+.5)-R) && xp(i)<(F*(j+.5)+R) && ((R-h)^2-(xp(i)-
F*(j+.5))^2) >= 0
tool(i,j) = -sqrt(R^2-(xp(i)-F*(j+.5))^2)+R;
surf(i,j) = -sqrt((R-h)^2-(xp(i)-F*(j+.5))^2)+R;
else
tool(i,j) = NaN;
surf(i,j) = NaN;
end
if tool(i,j) > doc*1.05
tool(i,j) = NaN;
end
if surf(i,j) > doc*1.05
surf(i,j) = NaN;
end

%creating new workpiece surface

%creating a line drawn from the center of the current toolpass radius
%to the beginning of non-hydrostatic pressure on the toolpass aka the
%beginning of the sideflow chip element

```



```

angle(i,j) = R-(xp(i)-F*(j+.5))/tan(-ltheta(t));

%creates a x for plotting only relevant values of angle
if angle(i,j) < doc && angle(i,j) > -.15
xpangle(i,j) = xp(i);
ypangle(i,j) = angle(i,j);
else
xpangle(i,j) = NaN;
ypangle(i,j) = NaN;
end

if surface(i,j) > tool(i,j) && surface(i,j) < surf(i,j) && pk == 0 &&
angle(i,j) < tool(i,j)
sideflowint = sideflowint + surface(i,j) - tool(i,j);
sideflowintcount = sideflowintcount + 1;
end
% determining start of length to multiply average sideflow chip value
over
if sideflowintcount == 1
sideflowstartx = xp(i);
sideflowstarty = surface(i,j);
end

if sideflowintcount > 1 && surf(i,j) < surface(i,j) && pk == 0
sideflowstopx = xp(i);
sideflowstopy = surf(i,j);
stopi = i;
pk=1;

%sideflow length has been verified graphically
THsideflowarealengthx(t,j) = sideflowstopx-sideflowstartx;

%sideflow tot has been verified graphically
sideflowtot(t,j) =
sideflowint/sideflowintcount*THsideflowarealengthx(t,j);

end

end

% announcing failure and skipping to next tool
if pk == 0
fprintf('Failure to generate sideflow volume in previous pass OR The
entire uncut chip thickness is less than hmin. \rIncrease model
resolution to get results that are near kinematic roughness. \r')
skip = 1;
else
% NEW SURFACE
% %%%%%%%%%%%%%%%%%%%%%%%%%%%%%%%%%%%%%%%%%%%%%%%%%%%%%%%%%%
for i = 1:profileres

```

```

%calculating sideflow extension and surface of the previous pass, hence
%the need for the above if statement.

% ir is the reverse of i, allowing for easier integration of the volume
% that is moving right to left
ir = profileres-i+1;
if tool(ir,j) >= surface(ir,j) && pk2 == 1 && surface(ir,j) < doc
sideflowextgapheight = tool(ir,j)-surface(ir,j);
sideflowextlength = xp(ir)-sideflowstartx;
sideflowextint = sideflowextint + sideflowextgapheight;
sideflowextintcount = sideflowextintcount + 1;

sideflowextgapvoltemp = -
sideflowextint/sideflowextintcount*sideflowextlength;

% moves to the next if statement when
% sideflow volume exceeds the susceptible
% region's volume
if sideflowextgapvoltemp >= sideflowtot(t,j)
sideflowextgapvol(t,j) = sideflowextgapvoltemp;
pk2=2;

end
% gets the i that occurs at the feed
% centermark. Useful for indexing profiles.
if tool(ir,j) < tool(ir-1,j)
Feedcenteri(j) = ir;
end
end
% Determines how far up the tool in the feed direction that the flow
% will slip due to the loss of the side flow chip
if pk2 == 2
% Sideflowtheoreticalstop
SFTSx = sideflowstopx;
SFTSTRACKi(j) = ir;

% Sideflow real peak
SFRPx = xp(ir);
SFRPy = tool(ir,j);
SFRPTRACKx(j) = SFRPx;
SFRPTRACKy(j) = SFRPy;
SFRPa = atan(((SFRPx-F*(j+.5))/(R-SFRPy)));

% Side flow real stop
SFRSa = (-ltheta(t)-SFRPa)-ltheta(t);
SFRSx = R*sin((-ltheta(t)-SFRPa)-ltheta(t))+F*(j+.5);
SFRSy = R - (R-h)*cos((-ltheta(t)-SFRPa)-ltheta(t));
% Sideflowrealstart (based on the volume of triangle it would take
% to achieve the same area taken away past the start of theoretical
% side flow chip thickness.

% simply the y value at the point found above

if SFRPy >= doc
skip = 1;

```

```

end

rchangeperang = h/(SFRSa-SFRPa);

% Modified length of the deformed sideflow
% volume
REALsideflowlength(t,j) = ((SFRPx-SFRSx)^2+(SFRPy-SFRSy)^2)^.5;
THsideflowlength(t,j) = ((SFRSx-sideflowstartx)^2+(SFRSy-
sideflowstarty)^2)^.5;
Sideflowstrain(t,j) = REALsideflowlength(t,j)/THsideflowlength(t,j);
Thermaleffect(t,1) =
REALsideflowlength(t,j)*Sideflowstrain(t,j)*13/13/F;

pk2 = 3;

end
%line equation creation'

end
if pk2 == 3
for k = 1:profileres
if xp(k) <= SFRPx
surface(k,j+1) = surface(k,j);
elseif xp(k) < SFRSx && xp(k) > SFRPx
currentang = atan((xp(k-1)-F*(j+.5))/(R-surface(k-1,j+1)));
angdiff = currentang - SFRPa;
surface(k,j+1) = -sqrt((R-angdiff*rchangeperang)^2-(xp(k)-
F*(j+.5))^2)+R;
else
surface(k,j+1) = surf(k,j);
if surface(k,j+1)>doc || isnan(surface(k,j+1))
surface(k,j+1)=doc;
end
end

% diagnosis of imaginary num issue
if 0 == isreal(surface)
fprintf('Imaginary number encountered \r')
skip = 1;
break

end
end
else
skip = 1;
fprintf('Skipping this condition due to pure burnishing condition\r')
break
end

end

```

```

%checker
figure(999)
hold off
subplot(2,1,1)
plot(xp,surf(:,j),xp,tool(:,j),xp,surface(:,j),sideflowstartx,sideflows
tarty,'o',sideflowstopx,sideflowstopy,'x',SFRPx,SFRPy,'o',SFRSx,SFRSy,'
x')
subplot(2,1,2)
plot(xp,surf(:,j),xp,tool(:,j),xp,surface(:,j+1),SFRPx,SFRPy,'o',SFRSx,
SFRSy,'x')

%if the last 20 of the SFRPTRACKy values are level, then exit loop to
%save time
if j >= 51 %does at least 20 loops
shortavg = mean(SFRPTRACKy((j-3:j)));
longavg = mean(SFRPTRACKy((j-50:j)));
if shortavg >=longavg*.995 && shortavg <=longavg*1.005
startiroughpre = Feedcenteri(j-35);
startirough = Feedcenteri(j-25);
stopirough = Feedcenteri(j-12);
%Sideflow smoothing multiplier. Everything should be smoother for
%higher values of this because the peaks are very tall and
%to the antifeed side of the tool
psharp(t) = SFRPa;
jhigh = j;
break
end
end
end

end

if skip == 1
RaModel(t,1) = NaN;
RzModel(t,1) = NaN;
RaTh(t,1) = NaN;
RzTh(t,1) = NaN;
RaTh(t,1) = F^2/R/32*1000;
RaBrammertz(t,1) =
(doe(t,2)^2/doe(t,1)/32+h/2*(1+h*doe(t,1)/(doe(t,2))^2))*1000;
else
%calculation of surface roughness
RaTh(t,1) = F^2/R/32*1000;
RzTh(t,1) = F^2/R/8*1000;
RaBrammertz(t,1) =
(doe(t,2)^2/doe(t,1)/32+h/2*(1+h*doe(t,1)/(doe(t,2))^2))*1000;

roughcurve = surface((1:stopirough),j);
rcx = xp((1:stopirough));

roughcurvepreseg = roughcurve((startiroughpre:stopirough));
rcpsx = rcx((startiroughpre:stopirough));
preseglength = length(roughcurvepreseg);

```

```

roughcurvepreseg_mean = mean(roughcurvepreseg);
roughcurvepreseg_zeroed = roughcurvepreseg-roughcurvepreseg_mean;
% Smoothing the resultant curve
roughcurvesmoothpreseg = filter(yg, 1 ,roughcurvepreseg_zeroed);
% Shortening to actual evaluation length
roughcurvesmoothrealseg = roughcurvesmoothpreseg((preseglength-
(stopirough-startirough)):preseglength);
rcrsrx = rcx((preseglength-(stopirough-startirough)):preseglength);

%Finding values for peak and valley (Rz/Rt evaluation)
Peak = max(roughcurvesmoothrealseg);
Valley = min(roughcurvesmoothrealseg);
% Calculating the mean surface height (Ra evaluation)
surfacemean(t) = mean(roughcurvesmoothrealseg);
% Calculating the deviation from the average surface height at
% each point
roughzfunc = abs(roughcurvesmoothrealseg-surfacemean(t));
% Mean of the deviation from the average surface height
RaModel(t,1) = mean(roughzfunc)*1000;
% Distance from the highest peak to the lowest along evaluation
% length (Rz = Rt because it is a model)
RzModel(t,1) = (Peak-Valley)*1000;
% Kinematic equations for Rz/Rt and Ra, as well as Brammertz's
% equation

% Creating the geometry for subsurface characteristic
% derivation

% the yg filter creates an offset, calculated here, to be used
% subsequently in xp
gioffset = ceil(length(yg)/2);

roughcurvesmoothrealseginplace = roughcurvesmoothrealseg +
roughcurvepreseg_mean;

subxp(1:profileres,1:jhigh-12)=NaN;
subsurface(1:profileres,1:jhigh-12)=NaN;
%Loop to create workpiece subsurface model
tpcount = 0;
totalplough = 0;

for j = jhigh-30:jhigh-12
cv = 0;
subtool(1:profileres,j)=NaN;
subsurf(1:profileres,j)=NaN;

for i = (startirough:stopirough)

if (R)^2-(xp(i)-smoothlength/2-F*(j)+F/2)^2>0
subsurface(i,j) = -sqrt((R)^2-(xp(i)-smoothlength/2-F*(j)+F/2)^2) + (R
- 0);

if subsurface(i,j)>=roughcurvesmoothrealseginplace(i-startirough +1)
subsurface(i,j) = NaN;

```

```

end
if subsurface(i,j)<=roughcurvesmoothrealseginplace(i-startirough +1)
totalplough = totalplough - subsurface(i,j)+
roughcurvesmoothrealseginplace(i-startirough +1);
tpcount = tpcount + 1;
end
end

% creating tool(i,j) geometry for this pass
if (R^2-(xp(i)-smoothlength/2-F*(j)+F/2)^2) >= 0 && ((R-
hmin(hone_r))^2-(xp(i)-smoothlength/2-F*(j)+F/2)^2) >= 0
subtool(i,j) = -sqrt(R^2-(xp(i)-smoothlength/2-F*(j)+F/2)^2)+R;
subsurf(i,j) = -sqrt((R-hmin(hone_r))^2-(xp(i)-smoothlength/2-
F*(j)+F/2)^2)+R;
else
subtool(i,j) = NaN;
subsurf(i,j) = NaN;
end
if subtool(i,j) > doc*.1
subtool(i,j) = NaN;
end
if subsurf(i,j) > doc*.1
subsurf(i,j) = NaN;
end

end
end

% gives the ploughed volume per mm
Mechanicaleffect(t,1) = totalplough/13/F;

figure(16)
clf
hold on
plot(xp(startirough:stopirough),subsurface(startirough:stopirough,:), '-
-', 'Linewidth',3, 'color',[0 0 0])
plot(xp(startirough:stopirough),roughcurvesmoothrealseginplace, 'Linewid
th',3, 'color',[0, 0.4470,
0.7410])%xp(startirough:stopirough),subtool((startirough:stopirough),j)
,

% set(gcf, 'Color', 'None');
% set(gca, 'Color', 'None');
% set(gcf, 'units', 'inches', 'position', [1,1,14,5])
xlim([3 3.5])
ylim([-0.004 .005])
set(gca, 'FontSize',16)
xlabel('Feed mm', 'fontname', 'Arial', 'FontSize', 24)
ylabel('Depth of Cut mm', 'fontname', 'Arial', 'FontSize', 24)
% axis equal

% plots every profile generated for a given condition
figure(5)
gridsize1 = ceil(sqrt(res));
gridsize2 = ceil(res/gridsize1);
subplot(gridsize2,gridsize1,figur)

```

```

plot(xp,surface(:,1),xp,surface(:,jhigh),xp(startirough-
gioffset:stopirough-gioffset),roughcurvesmoothrealseginplace)
%axis equal
legend('Pass 1','End pass')
ylim([-0.02 inf])

end

if skip == 0
Profilematrix(1:(1-startirough+stopirough),-1+(t)*3)=xp(startirough-
gioffset:stopirough-gioffset);
Profilematrix(1:(1-startirough+stopirough),(t)*3)=
roughcurvesmoothrealseg;
Profilematrix(1,-2+(t)*3) = t;

end

end

% Settings Documentation
Model8_fullfactorial{noselevels+3,1}="User Inputs:";
Model8_fullfactorial{noselevels+4,1}="Yeff Critical";
Model8_fullfactorial{noselevels+4,2}="Profile Resolution";
Model8_fullfactorial{noselevels+4,3}="Upper Feed Limit";
Model8_fullfactorial{noselevels+4,4}="Lower Feed Limit";
Model8_fullfactorial{noselevels+6,1}="DOC";
Model8_fullfactorial{noselevels+10,1}="Model Tweaks:";
Model8_fullfactorial{noselevels+11,1}="Smoothing window equation";
Model8_fullfactorial{noselevels+11,2}="DMTE damping equation";

Model8_fullfactorial{noselevels+5,1}=criteyeff;
Model8_fullfactorial{noselevels+5,2}=profileres;
Model8_fullfactorial{noselevels+5,3}=upfeed;
Model8_fullfactorial{noselevels+5,4}=lowfeed;
Model8_fullfactorial{noselevels+7,1}=doc;
Model8_fullfactorial{noselevels+12,1}=smoothlengthchar;
Model8_fullfactorial{noselevels+12,2}=DMTEdampedchar;

for y = 1:10
for e = 1:4
Model8_fullfactorial_Profiles{(noselevels+2+y),e}=Model8_fullfactorial{
(noselevels+2+y),e};
end
end

%organizing and labelling of data into one file
Model8_fullfactorial{nose_r+1,hone_r+1}{1,1} = 'LogFeed';
Model8_fullfactorial{nose_r+1,hone_r+1}{2,1} = doe(:,2);
Model8_fullfactorial{nose_r+1,hone_r+1}{1,2} = 'Ra Kinematic';
Model8_fullfactorial{nose_r+1,hone_r+1}{2,2} = RaTh(:,1);
Model8_fullfactorial{nose_r+1,hone_r+1}{1,3} = 'Rz Kinematic';
Model8_fullfactorial{nose_r+1,hone_r+1}{2,3} = RzTh(:,1);
Model8_fullfactorial{nose_r+1,hone_r+1}{1,4} = 'Ra Brammertz';
Model8_fullfactorial{nose_r+1,hone_r+1}{2,4} = RaBrammertz(:,1);
Model8_fullfactorial{nose_r+1,hone_r+1}{1,5} = 'Ra Model';

```

```

Model8_fullfactorial{nose_r+1,hone_r+1}{2,5} = RaModel(:,1);
Model8_fullfactorial{nose_r+1,hone_r+1}{1,6} = 'Rz Model';
Model8_fullfactorial{nose_r+1,hone_r+1}{2,6} = RzModel(:,1);
Model8_fullfactorial{nose_r+1,hone_r+1}{1,7} = 'Rz Model with DMTE';
Model8_fullfactorial{nose_r+1,hone_r+1}{2,7} =
RzModel(:,1)+DMTEdamped(hone_r);
Model8_fullfactorial{nose_r+1,hone_r+1}{1,8} = 'Mechanical Effect';
Model8_fullfactorial{nose_r+1,hone_r+1}{2,8} = Mechanicaleffect(:,1);
Model8_fullfactorial{nose_r+1,hone_r+1}{1,9} = 'Thermal Effect';
Model8_fullfactorial{nose_r+1,hone_r+1}{2,9} = Thermaleffect(:,1);
Model8_fullfactorial_Profiles{nose_r+1,hone_r+1} = Profilematrix;

figure(nose_r)
clf
loglog(Model8_fullfactorial{nose_r+1,hone_r+1}{2,3},Model8_fullfactoria
l{nose_r+1,hone_r+1}{2,3},'HandleVisibility','off','color',[0 0 0])
hold on
%plotting the unadjusted model R_ vs Feed
loglog(Model8_fullfactorial{nose_r+1,hone_r+1}{2,3},Model8_fullfactoria
l{nose_r+1,hone_r+1}{2,6},'HandleVisibility','off')
% %plotting the MTE-adjusted model R_ vs Feed
%
loglog(Model8_fullfactorial{nose_r+1,hone_r+1}{2,3},Model8_fullfactoria
l{nose_r+1,hone_r+1}{2,7},'HandleVisibility','off')
end
end

set(gca,'FontSize',16)
xlabel('f^2/r_c*8 μm','fontname','Arial','FontSize',24)
ylabel('R_z μm','fontname','Arial','FontSize',24)

```


REFERENCES

1. Jawahir, I., et al., *Surface integrity in material removal processes: Recent advances*. CIRP annals, 2011. **60**(2): p. 603-626.
2. Field, M., K. JF, and C. JT, *A review of measuring methods for surface integrity*. 1972.
3. Vollertsen, F., et al., *Size effects in manufacturing of metallic components*. CIRP Annals, 2009. **58**(2): p. 566-587.
4. Childs, T., et al., *The influence of cutting edge sharpness on surface finish in facing with round nosed cutting tools*. 2008.
5. Moll, H., *Die Herstellung hochwertiger Drehflächen : Einfluß der Schnittbedingungen auf die Oberflächengüte beim Drehen, Schlichten und Feinschlichten*. 1940, VDI-Verl.: Berlin.
6. Sokolowski, A., *Präzision in der Metallbearbeitung*, VEB-Verlag Technik. 1955, Berlin.
7. Albrecht, P., *New Developments in the Theory of the Metal-Cutting Process: Part I. The Ploughing Process in Metal Cutting*. Journal of Engineering for Industry, 1960. **82**(4): p. 348-357.
8. Ikawa, N., S. Shimada, and H. Tanaka, *Minimum thickness of cut in micromachining*. Nanotechnology, 1992. **3**(1): p. 6-9.
9. Brammertz, P., *Die entstehung der oberflächenrauheit beim feindreihen*. Industrie Anzeiger, 1961. **2**: p. 25-32.
10. Yuan, Y., et al., *Surface roughness modeling in micro end-milling*. The International Journal of Advanced Manufacturing Technology, 2017. **95**(5-8): p. 1655-1664.
11. Grzesik, W., *A revised model for predicting surface roughness in turning*. Wear, 1996. **194**(1-2): p. 143-148.
12. Childs, T., et al., *Surface finishes from turning and facing with round nosed tools*. CIRP annals, 2008. **57**(1): p. 89-92.
13. Knuefermann, M.M., *Machining surfaces of optical quality by hard turning*. 2003.
14. Shaw, M.C. and J. Cookson, *Metal cutting principles*. Vol. 2. 2005: Oxford university press New York.
15. Lambert, H., *Two years of finish-turning research at the Technological University, Delft*. Ann. CIRP, 1961. **10**: p. 246-255.
16. Brown, I. and J. Schoop, *An Iterative Size Effect Model of Surface Generation in Finish Machining*. Journal of Manufacturing and Materials Processing, 2020. **4**(3): p. 63.
17. Sata, T., *Surface finish in metal cutting*. Annals of the CIRP, 1964: p. 190-197.
18. Pekelharing, A. and C. Gieszen, *Material side flow in finish turning*. Annals of the CIRP, 1971. **20**(1): p. 21-22.
19. El-Wardany, T. and M. Elbestawi, *Phenomenological analysis of material side flow in hard turning: causes, modeling, and elimination*. Machining Science and Technology, 1998. **2**(2): p. 239-251.
20. Liu, K., *Process modeling of micro-cutting including strain gradient effects*, S.N. Melkote, Editor. 2005, ProQuest Dissertations Publishing.

21. Kishawy, H.A., A. Haglund, and M. Balazinski, *Modelling of Material Side Flow in Hard Turning*. CIRP Annals, 2006. **55**(1): p. 85-88.
22. Kishawy, H.A. and M.A. Elbestawi, *Effects of process parameters on material side flow during hard turning*. International Journal of Machine Tools and Manufacture, 1999. **39**(7): p. 1017-1030.
23. Liu, K. and S.N. Melkote, *Effect of plastic side flow on surface roughness in micro-turning process*. International Journal of Machine Tools and Manufacture, 2006. **46**(14): p. 1778-1785.
24. Özel, T., T.-K. Hsu, and E. Zeren, *Effects of cutting edge geometry, workpiece hardness, feed rate and cutting speed on surface roughness and forces in finish turning of hardened AISI H13 steel*. The International Journal of Advanced Manufacturing Technology, 2005. **25**(3): p. 262-269.
25. Özel, T. and Y. Karpat, *Predictive modeling of surface roughness and tool wear in hard turning using regression and neural networks*. International Journal of Machine Tools and Manufacture, 2005. **45**(4): p. 467-479.
26. Thiele, J.D. and S. N. Melkote, *Effect of cutting edge geometry and workpiece hardness on surface generation in the finish hard turning of AISI 52100 steel*. Journal of Materials Processing Tech, 1999. **94**(2): p. 216-226.
27. Zhao, T., et al., *Effect of cutting edge radius on surface roughness and tool wear in hard turning of AISI 52100 steel*. The International Journal of Advanced Manufacturing Technology, 2017. **91**(9-12): p. 3611-3618.
28. Mai, Q., et al., *A new geometrical model of the formation of machined surface*. The International Journal of Advanced Manufacturing Technology, 2017. **91**(9-12): p. 3493-3502.
29. Schultheiss, F., et al., *Influence of the Minimum Chip Thickness on the Obtained Surface Roughness During Turning Operations*. Procedia CIRP, 2014. **13**: p. 67-71.
30. Kountanya, R., *Surface Finish and Tool Wear Characterization in Hard Turning Using a Mathematical Cutting Tool Representation*. Machining Science and Technology, 2011. **15**(4): p. 429-452.
31. Aouici, H., et al., *Analysis of surface roughness and cutting force components in hard turning with CBN tool: Prediction model and cutting conditions optimization*. Measurement, 2012. **45**(3): p. 344-353.
32. Abbas, A.T., et al., *Artificial intelligence monitoring of hardening methods and cutting conditions and their effects on surface roughness, performance, and finish turning costs of solid-state recycled Aluminum alloy 6061 chips*. Metals, 2018. **8**(6): p. 394.
33. Yang, A., et al., *Optimum surface roughness prediction for titanium alloy by adopting response surface methodology*. Results in Physics, 2017. **7**: p. 1046-1050.
34. Zong, W., et al., *Conservation law of surface roughness in single point diamond turning*. International Journal of Machine Tools and Manufacture, 2014. **84**: p. 58-63.
35. Chen, J. and Q. Zhao, *A model for predicting surface roughness in single-point diamond turning*. Measurement, 2015. **69**: p. 20-30.

36. He, C.L., W.J. Zong, and T. Sun, *Origins for the size effect of surface roughness in diamond turning*. International Journal of Machine Tools and Manufacture, 2016. **106**: p. 22-42.
37. Lin, S.C. and M.F. Chang, *A study on the effects of vibrations on the surface finish using a surface topography simulation model for turning*. International Journal of Machine Tools and Manufacture, 1998. **38**(7): p. 763-782.
38. Zhang, S., et al., *A review of machine-tool vibration and its influence upon surface generation in ultra-precision machining*. International journal of machine tools and manufacture, 2015. **91**: p. 34-42.
39. Altintas, Y. and M. Weck, *Chatter stability of metal cutting and grinding*. CIRP annals, 2004. **53**(2): p. 619-642.
40. Biermann, D. and A. Baschin, *Influence of cutting edge geometry and cutting edge radius on the stability of micromilling processes*. Production Engineering, 2009. **3**(4-5): p. 375.
41. Yusoff, A.R., et al., *The role of tool geometry in process damped milling*. The International Journal of Advanced Manufacturing Technology, 2010. **50**(9-12): p. 883-895.
42. Budak, E. and L.T. Tunc, *Identification and modeling of process damping in turning and milling using a new approach*. CIRP Annals, 2010. **59**(1): p. 403-408.
43. Henriksen, E.K. *Residual stresses in machined surfaces*. 1948. ASME.
44. Field, M. and J. Kahles, *The surface integrity of machined-and ground high-strength steels(Surface integrity of machined and ground high strength steels)*. 1964., 1964: p. 54-77.
45. Field, M. and J.F. Kahles, *Review of surface integrity of machined components*. Annals of the CIRP, 1971. **20**(2): p. 153-163.
46. Bailey, J. and S. Jeelani, *Surface integrity in machining 18% nickel maraging steel*. ASME Transactions, 1974: p. 74-185.
47. Bailey, J. and S. Jeelani, *Determination of subsurface plastic strain in machining using an embossed grid*. Wear, 1976. **36**(2): p. 199-206.
48. Liu, C. and M. Barash, *The mechanical state of the sublayer of a surface generated by chip-removal process—Part 1: Cutting with a sharp tool*. 1976.
49. Liu, C. and M. Barash, *The mechanical state of the sublayer of a surface generated by chip-removal process—part 2: cutting with a tool with flank wear*. 1976.
50. Griffiths, B., *Mechanisms of white layer generation with reference to machining and deformation processes*. 1987.
51. Jeelani, S. and J. Bailey, *Residual stress distribution in machining annealed 18 percent nickel maraging steel*. 1986.
52. Tönshoff, H.K. and E. Brinksmeier, *Determination of the Mechanical and Thermal Influences on Machined Surfaces by Microhardness and Residual Stress Analysis*. CIRP Annals, 1980. **29**(2): p. 519-530.
53. Griffiths, B., *Manufacturing surface technology: surface integrity and functional performance*. 2001: Elsevier.
54. Rech, J., H. Hamdi, and S. Valette, *Workpiece surface integrity*, in *Machining*. 2008, Springer. p. 59-96.

55. Ulutan, D. and T. Ozel, *Machining induced surface integrity in titanium and nickel alloys: A review*. International Journal of Machine Tools and Manufacture, 2011. **51**(3): p. 250-280.
56. Griffiths, B. and D. Furze, *Tribological advantages of white layers produced by machining*. 1987.
57. Simes, T., S. Mellor, and D. Hills, *A note on the influence of residual stress on measured hardness*. The Journal of Strain Analysis for Engineering Design, 1984. **19**(2): p. 135-137.
58. Pharr, G., et al., *Effects of residual stress on the measurement of hardness and elastic modulus using nanoindentation*. MRS Online Proceedings Library Archive, 1994. **338**.
59. Lee, Y.-H. and D. Kwon, *Estimation of biaxial surface stress by instrumented indentation with sharp indenters*. Acta Materialia, 2004. **52**(6): p. 1555-1563.
60. Griffiths, B., *White layer formations at machined surfaces and their relationship to white layer formations at worn surfaces*. 1985.
61. El-Wardany, T.I., H.A. Kishawy, and M.A. Elbestawi, *Surface Integrity of Die Material in High Speed Hard Machining, Part 2: Microhardness Variations and Residual Stresses*. Journal of Manufacturing Science and Engineering, 1999. **122**(4): p. 632-641.
62. Enrique-Jimenez, P., et al., *Mapping the Mechanical Properties of Poly(3-hydroxybutyrate-co-3-hydroxyvalerate) Banded Spherulites by Nanoindentation*. Polymers (Basel), 2016. **8**(10).
63. Warren, A. and Y. Guo, *Machined surface properties determined by nanoindentation: Experimental and FEA studies on the effects of surface integrity and tip geometry*. Surface and Coatings Technology, 2006. **201**(1-2): p. 423-433.
64. Biondani, F.G. and G. Bissacco, *Effect of cutting edge micro geometry on surface generation in ball end milling*. CIRP Annals, 2019. **68**(1): p. 571-574.
65. Liu, X., R.E. DeVor, and S.G. Kapoor, *An Analytical Model for the Prediction of Minimum Chip Thickness in Micromachining*. Journal of Manufacturing Science and Engineering, 2006. **128**(2).
66. Ståhl, J.E., F. Schultheiss, and S. Hägglund, *Analytical and Experimental Determination of the Ra Surface Roughness during Turning*. Procedia Engineering, 2011. **19**: p. 349-356.
67. Arcona, C. and T.A. Dow, *An empirical tool force model for precision machining*. 1998.
68. Maiss, O., T. Grove, and B. Denkena, *Influence of asymmetric cutting edge roundings on surface topography*. Production Engineering, 2017. **11**(4-5): p. 383-388.
69. De Oliveira, F.B., et al., *Size effect and minimum chip thickness in micromilling*. International Journal of Machine Tools and Manufacture, 2015. **89**: p. 39-54.
70. Challen, J. and P. Oxley, *Slip-line fields for explaining the mechanics of polishing and related processes*. International Journal of Mechanical Sciences, 1984. **26**(6-8): p. 403-418.
71. Malekian, M., et al., *Modeling of minimum uncut chip thickness in micro machining of aluminum*. Journal of Materials Processing Technology, 2012. **212**(3): p. 553-559.

72. Outeiro, J.C., *Influence of tool sharpness on the thermal and mechanical phenomena generated during machining operations*. International Journal of Machining and Machinability of Materials, 2007. **2**(3-4): p. 413-432.
73. DUCOBU, F., E. FILIPPI, and E. RIVIÈRE-LORPHEVRE. *Modélisation de l'influence de la profondeur de coupe en micro-coupe orthogonale*. in *Congrès français de mécanique*. 2009. AFM, Maison de la Mécanique, 39/41 rue Louis Blanc-92400 Courbevoie.
74. Hashimoto, F., Y.B. Guo, and A.W. Warren, *Surface Integrity Difference between Hard Turned and Ground Surfaces and Its Impact on Fatigue Life*. CIRP Annals, 2006. **55**(1): p. 81-84.
75. Krolczyk, G., P. Nieslony, and S. Legutko, *Microhardness and Surface Integrity in Turning Process of Duplex Stainless Steel (DSS) for Different Cutting Conditions*. Journal of Materials Engineering and Performance, 2013. **23**(3): p. 859-866.
76. Pawade, R.S., S.S. Joshi, and P.K. Brahmankar, *Effect of machining parameters and cutting edge geometry on surface integrity of high-speed turned Inconel 718*. International Journal of Machine Tools and Manufacture, 2008. **48**(1): p. 15-28.
77. Denkena, B., T. Grove, and O. Maiss, *Influence of the cutting edge radius on surface integrity in hard turning of roller bearing inner rings*. Production Engineering, 2015. **9**(3): p. 299-305.

VITA

Ian Brown was born in 1994 in Paducah, Kentucky. Following his high school education at Caldwell County High, he pursued a Bachelor of Science in Mechanical Engineering at the University of Kentucky, working as an Engineering Assistant at Belcan Inc. during his final two undergraduate years. After completion of this degree, he joined Dr. Julius Schoop's research group to pursue a Master of Science in Mechanical Engineering at the University of Kentucky.

LIST OF PUBLICATIONS

1. Brown, Ian, and Julius Schoop. "An Iterative Size Effect Model of Surface Generation in Finish Machining." *Journal of Manufacturing and Materials Processing* 4.3 (2020): 63.
2. Brown, Ian, and Julius Schoop. "The effect of cutting edge geometry, nose radius and feed on surface integrity in finish turning of Ti-6Al4V." *Procedia CIRP* 87 (2020): 142-147.
3. Schoop, Julius, David Adeniji, and Ian Brown. "Computationally efficient, multi-domain hybrid modeling of surface integrity in machining and related thermomechanical finishing processes." *Procedia CIRP* 82 (2019): 356-361.